

**UCSF**

**UC San Francisco Electronic Theses and Dissertations**

**Title**

Engineering cell-cell interaction to improve antigen sensitivity of CAR-T cells

**Permalink**

<https://escholarship.org/uc/item/5jx8c29q>

**Author**

Kim, Ki Hyun

**Publication Date**

2023

Peer reviewed|Thesis/dissertation

Engineering cell-cell interaction to improve antigen sensitivity of CAR-T cells

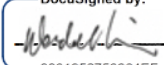
by  
Ki Kim

DISSERTATION  
Submitted in partial satisfaction of the requirements for degree of  
DOCTOR OF PHILOSOPHY

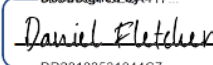
in  
Pharmaceutical Sciences and Pharmacogenomics

in the  
GRADUATE DIVISION  
of the  
UNIVERSITY OF CALIFORNIA, SAN FRANCISCO

Approved:

DocuSigned by:  
  
3901952758864EF... Wendell Lim  
Chair

DocuSigned by:  
  
DocuSigned by: 417... Tejal Desai

DocuSigned by:  
  
DD28103531044C7... Daniel Fletcher

\_\_\_\_\_  
\_\_\_\_\_  
Committee Members

Copyright 2023

By

Ki Kim

## **Acknowledgments**

My Ph.D. would not have been possible without the incredible help and support I have received throughout my journey. First and foremost, I would like to thank my family who has sacrificed so much so that I can continue doing what I love. I know the past several years have been especially difficult for everyone in my family, but I want to thank them for not giving up and doing everything they can to make the situation better for all of us. I am so fortunate to have my family and am excited to spend the next couple of years together.

Next, I would like to thank my thesis advisor Wendell Lim for giving me this amazing opportunity to work in his lab for the past 6 years. I still remember the day when you finally let me join the lab. I can almost guarantee I was the happiest first-year student. Throughout the years, I really learned a lot from Wendell as both a scientist and visionary. Even after 6 years of working with you, I am still amazed by your ability to think outside the box and continue to innovate year after year. Through consistently setting high standards for the quality of my work and providing the necessary resources and support to achieve each task, I have experienced tremendous growth and learning as a scientist.

I cannot give enough thanks to Noleine Blizzards for making this all possible. Noleine was the number one person I went to for help. And she always had the right answers for me. Noleine, you are an amazing person, and you probably know that already. Thank you so much for all your support throughout the years. I already know I am going to miss you.

I would also like to thank both my thesis committee members, Tejal Desai and Dan Fletcher for their guidance and helpful discussions. They always made time to talk to me when I need advice on my project and my career choice. I simply could not have asked for a better thesis committee.

Next, I would like to thank my everyday mentors, Adam Stevens and Josiah Gerdst, and Ricardo Almeida. I really really enjoyed talking science with you guys. Both of you have taught me so much how to become a better scientist. I will not forget all the ate night tissue cultures we had together. Thank you for being my mentor and my friend. I really enjoyed your companionship, and I look forward to working with both of you in the future.

I would like to thank all the physician-scientists in the lab, Greg Allen, Josiah Gerdst and Phil Pauerstein not only for sharing the nuances of treating patients with new technology such as CAR-T therapy but also for giving me countless free consultations.

Pilar Lopez and Sim Sidhu, thank you so much for managing our lab so well. I sometimes forget how much work you guys do for the lab so that we can focus on our projects. Running into you guys in the lab always made me laugh. Thank you so much for providing such care for the lab. I really appreciated your friendship and support.

I would also like to thank Wei Yu and Yurie Tonia for their help in doing mouse work. Without their help, I could not have generated all the in-vivo data that is crucial for my thesis.

I would also like to give thanks to Emre Toner and Adrian Barrera-Velasquez for various help in carrying out experiments for my thesis work, as well as their friendliness.

I would like to thank my fellow graduate students, Nish Reddy, Devan Shah, Hersh Bhargava, and Riley Stockard. I was so lucky to have you guys as my colleagues and friends. I wish I could forever work with you guys. Thank you so much for being such caring friends throughout the years.

Last but not least, I would like to thank my program, PSPG, and Rebecca Dawson for all the support they have given me.

## Contributions

*Portions of Chapter 2 have been submitted for publication as a scientific journal article:*

A. Stevens, A. Harris, J. Gerdts, **K. Kim**, C. Trentesaux, J. Ramirez, W. McKeithan, F.

O. Klein, D. Fletcher, W. Lim, *Programming multicellular assembly with synthetic cell adhesion molecules*, Nature, 2023

## **Abstract**

Engineering cell-cell interaction to improve antigen sensitivity of CAR-T cells

Ki Kim

Chimeric Antigen Receptor T cell (CAR-T) therapy has shown remarkable success in the treatment of hematological malignancies by reprogramming patients' own T cells to target cancer cells expressing specific antigens. However, CAR-T efficacy in solid tumors has been limited due to the difficulty of identifying a single antigen to differentiate tumor cells from healthy cells and the requirement for precise T cell-tumor cell interactions. Cell adhesion, a critical component of this interaction, plays a crucial role in governing the potency of CAR-T-mediated killing. We developed a novel synthetic receptor that can be used to program cell-cell interaction. Combined with chimeric receptors, we demonstrate the use case of a novel synthetic cell adhesion to improve the antigen sensitivity of CAR-T cells and further improve the specificity of the therapy.

This dissertation begins with the challenges in CAR T field that are currently limiting the efficacy of the treatment. I highlighted the both in-vitro and in-vivo instances where the current CAR T technology has diminished cytotoxicity against tumor cells. The importance of cell-cell adhesion and formation of immunological synapse is also discussed.



I present the discovery and characterization of synthetic cell-cell adhesion molecules in L929 fibroblast as a synthetic tool to direct cell-cell interaction. Lastly, I demonstrate how synthetic cell adhesion can exclude CD45 from the immunological synapse between the human primary T cells and tumor cells, resulting in increased antigen sensitivity of CAR T cells.

## Table of Contents

### Chapter 1-Introduction

..... 1

Reference

..... 7

### Chapter 2- Engineering synthetic adhesion molecules to program

cell-cell interaction

..... 12

Reference

..... 31

### Chapter 3 - Using synthetic adhesion molecules to enhance CAR-T therapy

..... 85

Reference

..... 93

### Chapter 4 - Concluding Remarks

..... 108

## List of Figures

### Chapter 2-Engineering synthetic adhesion molecules

Figure 2.1-Synthetic Cell Adhesion Molecules (synCAMs) facilitate custom cell-cell interaction .....	57
Figure 2.2-SynCAM intracellular domains yield interfaces with distinct mechanical and morphological properties .....	59
Figure 2.3- The balance of ICD properties determines asymmetric synCAM interface morphology .....	61
Figure 2.4- Programming custom multicellular assemblies with homotypic and heterotypic synCAMs .....	64
Figure 2.5- Using synCAMs to reshape tissue organization .....	65

Figure 2.6- Characterization of synCAM expression and function in L929 fibroblast cells	66
Figure 2.7- haracterization of NCAM-1 and Intb1 synCAM function across a series of affinities	68
Figure 2.8- Characterization of tuning synCAM expression	70
Figure 2.9- Differential sorting of synCAMs with varying ECD affinity and ICD	71
Figure 2.10- Cell spreading with alternative synCAMs	73
Figure 2.11- Quantification of synCAM cell spreading kinetics	74
Figure 2.12- Perturbation of synCAM morphology by small molecule inhibitors of specific actin regulator	75

Figure 2.13- Loss of function mutations in synCAM ICD .....	76
Figure 2.14- Asymmetric cell-cell interfaces: mismatched ICDs .....	78
Figure 2.15- Testing orthogonality of synCAM ECD pairs by sorting assays .....	79
Figure 2.16- Differential sorting of L929s with homophilic binding synCAMs .....	81
Figure 2.17- Targeting WT Pcad with synCAM .....	82
Figure 2.18- SynCAMs function in primary cells: mesenchymal stem cells (MSCs), dermal fibroblasts, and iPSC derived smooth muscle cells .....	83

### Chapter 3- Using synthetic adhesion molecules to enhance CAR-T therapy

Figure 3.1- Synthetic cell adhesion enhances CAR T cell killing of MCF7 breast cancer .....	100
Figure 3.2- SynNCAM binding facilitates CD45 exclusion .....	102
Figure 3.3-Synthetic adhesion enhances CAR-mediated killing in-vivo .....	104
Figure 3.4- SynCAM CAR T cells eliminate CAR-resistant tumors .....	106

## **Chapter 1- Introduction**

### **Abstract**

Cell-based therapy has shown great potential in treating blood tumors such as B-cell lymphoma. While there are ongoing efforts to further optimize and improve the CAR T cells to improve their efficacy and minimize side effects, there are a few areas in the field that require immediate attention to make CAR T cells applicable for more patients with different types of cancer. We outline various efforts in cell engineering field to address the problem of antigen escape that occurs in patients with targeted cell immunotherapies, and problems that CAR T cells have targeting tumor cells with target antigen that are expressed at low levels.

### **Challenges in engineering T cells to treat tumors with low target antigen density**

Chimeric Antigen Receptor T-cell (CAR-T) therapy has emerged as a promising treatment modality for cancer, harnessing the power of the immune system to target and eliminate tumor cells. However, challenges remain in optimizing CAR-T therapy's efficacy, particularly in enhancing tumor recognition and its efficacy against tumors with limited tumor antigens. This dissertation aims to explore novel strategies and approaches to improve the antigen sensitivity and specificity of CAR-T cells.

Recent data from both academic studies and clinical studies suggest that the efficacy of CAR-T therapy decreases dramatically with decreasing levels of target antigen for CARs(Heitzeneder et al., 2022; Majzner et al., 2020). These observations are especially critical in clinical settings because antigen escape has been reported as

one of the key challenges in CAR-T therapy where tumor cells downregulate the target antigen for CARs to avoid CAR-mediated cytotoxicity(Majzner & Mackall, 2018).

Over the past few years, various modifications have been made to the design of CARs to improve its toxicity and persistence(Pietrobon et al., 2021; Subklewe et al., 2019). These improvements have been demonstrated in both academic and clinical settings to show either increased cytotoxicity or persistence(Pietrobon et al., 2021; Ying et al., 2019). However, these modifications have not been able to show meaningful improvement in the antigen sensitivity of CARs (Burton et al., 2023; Schanda et al., 2021) In order to make next-generation CAR-T therapy more effective against various tumors with limited antigen expression, understanding and improving the antigen sensitivity of CAR-T cells will be critical.

## **Introduction**

### ***The important role of adhesion interaction plays in T cell***

T cells endogenous express various adhesion molecules that mediate the trafficking and activation of the cell (Bierer & Burakoff, 1988). Trafficking of T cells into tumors has been studied heavily to understand the mechanisms T cells utilize to home to the site of tumor cells. The process of T-cell trafficking is reported to be a dynamic process, involving a series of distinct processes, which include rolling, adhesion, extravasation, and chemotaxis(Slaney et al., 2014). Another area of high interest is role of adhesion molecules in forming functional immunological synapses between the T cells and tumor cells(Dustin, 2007). T cells endogenously express LFA-1 on the surface



are found in low-affinity in their resting state(Walling & Kim, 2018). LFA-1 integrin has two different conformations that can be induced to a high-affinity state from a low-affinity state by chemokine stimulations and inside-out signaling(Bleul et al., 1996; Constantin et al., 2000). This switch in affinity state allows T cells to adhere to the target cells with ICAM-1 as the target ligand for LFA-1, and either initiate crawling or formation of immunological synapses in TCR signaling (Graf et al., 2007). Combined with the interaction of another adhesion molecule found in T cells, CD2, T cells form well organized immunological synapse between the t cells and tumor cells where TCR microclusters are found in the center of the immunological synapse,cSMAC, surrounded by a distinct outer layer of LFA1:ICAM and CD2:CD48/CD59,pSMAC, pushing out CD45 phosphatase to most outer layer (Fritzsche et al., 2017).

While the role of adhesion in TCR signaling as well as CAR signaling has been regarded as an important factor in mediating T cell activation, leading to the effective killing of the target tumor cells, intricate mechanisms behind the roles of adhesion interaction in T cell activation in CAR-T cells still not fully understood.

### ***Understanding the difference between TCR and CAR***

Because CARs were designed after endogenous TCR, the difference between endogenous TCR and CAR has been often overlooked. However, recent studies point out a huge discrepancy in antigen sensitivity between the two receptors. In several studies CARs are reported to require 100 to 1000 times higher antigen density than TCRs to induce T cell activation (Gudipati et al., 2020; Harris et al., 2018; Salter et al., 2021). These observations potentially explain the occurrence of antigen escape in

lymphoma patients who were treated with high-affinity aCD19 CAR T cells(Ruella & Maus, 2016).

One potential explanation for such a discrepancy in antigen sensitivity between two receptors was demonstrated in a lipid-supported bilayer study where activation of T cells was measured in the presence and absence of different molecules T cells use to interact with the target cells. In the study, TCR-expressing T cells had 22-, 125- fold increase in antigen sensitivity in the presence of ICAM-1 and CD58 respectively on the lipid bilayer(Burton et al., 2023). In contrast, CAR-expressing T cells had only seen 1.4 to 4.7-fold increase in antigen sensitivity in the presence of ICAM-1 and CD58(Burton et al., 2023).

What is fascinating about this difference is that both of the molecules that led to a significant increase in antigen sensitivity of TCR are molecules that endogenous adhesion molecules use to adhere to the target cells(Quastel & Dustin, 2022; Reina & Espel, 2017). While we do not have a clear understanding of such discrepancy, one potential explanation could be found in the structural difference between the immunological synapse of TCRs and CARs. Teppert et. al. carefully studied the differences between the two receptors and found that there are structural differences in the immunological synapses of the two receptors(Teppert et al., 2022). Authors suggest that while TCRs are efficient in forming immunological synapse with distinct layers that compartmentalize TCR, adhesion, and CD45 phosphatase, CARs are not capable of reliably replicating this distinct structure of the immunological synapse. As a result, CD45 phosphatase, which is known to dephosphorylate ITAM regions in CD3zeta, is

not excluded from the CARs resulting in dampening of T cell activation when the CAR antigen is expressed at a low level on the tumor cells.

### ***Loss of adhesion molecules can lead to decreased CAR efficacy***

Alternative approaches in understanding and addressing antigen escape and decreased CAR-mediated cytotoxicity can be linked to the downregulation of adhesion molecules on the tumor sides. A recent study done by Larson et. al. looked at which surface proteins on the tumor cells led to the most significant decrease in CAR-mediated cytotoxicity(Larson et al., 2022). In their study, CRISPR knockout of IFN $\gamma$ R in solid tumors led to the most significant decrease in the CAR-mediated cytotoxicity next to the knockout of the target antigen for CARs. Furthermore, the authors studied which molecules are mediated in IFN $\gamma$  signaling and modulate CAR-mediated killing. Through blocking assay and further knockout studies, ICAM-1 adhesion was found to be the key molecule that was downregulated in the IFN $\gamma$ R KO solid tumors, suggesting that CAR-T cells have diminished efficacy against tumor cells that have downregulation of ICAM-1 adhesion molecules on the tumor cells. Additionally, loss or defects in IFN $\gamma$  signaling in different tumors have been associated with decreased efficacy in immunotherapies, suggesting a lack of IFN $\gamma$  signaling and adhesion molecules are correlated with not only CAR-T therapy but with broader types of immunotherapy(Duncan et al., 2007; Gao et al., 2016; Sceneay et al., 2019).

## ***Conclusion and outlook***

With increasing evidence behind the importance of adhesion interaction in CAR-mediated killing, and the inability of CAR-expressing T cells to exploit endogenous adhesion molecules, augmenting adhesion interaction between the CAR-T cells and the tumor cells may be beneficial in increasing antigen sensitivity of CAR-T cells. In this dissertation, the development and characterization of synthetic cell adhesion molecules are shown(Stevens et al., 2023). Furthermore, we demonstrate how these newly developed synthetic receptors can be used to augment adhesion interaction between CAR-T cells and tumor cells with low CAR antigen, resulting in increased antigen sensitivity and cytotoxicity

## References

Bierer, B. E. & Burakoff, S. J. T cell adhesion molecules. *The FASEB Journal*, 2(10), 2584–2590 (1988).

Bleul, C et al. A highly efficacious lymphocyte chemoattractant, stromal cell-derived factor 1 (SDF-1). *The Journal of Experimental Medicine*, 184(3), 1101–1109 (1996).

Burton, J. et al. Inefficient exploitation of accessory receptors reduces the sensitivity of chimeric antigen receptors. *Proceedings of the National Academy of Sciences*, 120(2), e2216352120 (2023).

Constantin, G et al. Chemokines Trigger Immediate  $\beta 2$  Integrin Affinity and Mobility Changes Differential Regulation and Roles in Lymphocyte Arrest under Flow. *Immunity*, 13(6), 759–769 (2000).

Duncan, T. et al. Loss of IFN $\gamma$  Receptor Is an Independent Prognostic Factor in Ovarian Cancer. *Clinical Cancer Research*, 13(14), 4139–4145(2007).

Dustin, M. L. Cell adhesion molecules and actin cytoskeleton at immune synapses and kinapses. *Current Opinion in Cell Biology*, 19(5), 529–533 (2007).

Fritzsche, M. et al. Cytoskeletal actin dynamics shape a ramifying actin network underpinning immunological synapse formation. *Science Advances*, 3(6), e1603032 (2017).

Gao, J. et al. Loss of IFN- $\gamma$  Pathway Genes in Tumor Cells as a Mechanism of Resistance to Anti-CTLA-4 Therapy. *Cell*, 167(2), 397-404 (2016).

Graf, B. et al. LFA-1-Mediated T Cell Costimulation through Increased Localization of TCR/Class II Complexes to the Central Supramolecular Activation Cluster and Exclusion of CD45 from the Immunological Synapse. *The Journal of Immunology*, 179(3), 1616–1624 (2007).

Gudipati, V et al. Inefficient CAR-proximal signaling blunts antigen sensitivity. *Nature Immunology*, 21(8), 848–856 (2020).

Harris, D. et al. Comparison of T Cell Activities Mediated by Human TCRs and CARs That Use the Same Recognition Domains. *The Journal of Immunology*, 200(3), 1088–1100 (2018).

Heitzeneder, S. et al. GPC2-CAR T cells tuned for low antigen density mediate potent activity against neuroblastoma without toxicity. *Cancer Cell*, 40(1), 53-69 (2022).

Larson, R. et al. CAR T cell killing requires the IFN $\gamma$ R pathway in solid but not liquid tumours. *Nature*, 604(7906), 563–570 (2022).

Majzner, R. G. & Mackall, C. L. Tumor Antigen Escape from CAR T-cell Therapy. *Cancer Discovery*, 8(10), 1219–1226 (2018).

Majzner, R. et al. Tuning the Antigen Density Requirement for CAR T-cell Activity. *Cancer Discovery*, 10(5), 702–723 (2020).

Pietrobon, V. Todd, L. A., Goswami, A., Stefanson, O., Yang, Z. & Marincola, F. Improving CAR T-Cell Persistence. *International Journal of Molecular Sciences*, 22(19), 10828 (2021).

Quastel, M. & Dustin, M. The CD58–CD2 axis in cancer immune evasion. *Nature Reviews Immunology*, 22(7), 409–409 (2022).

Reina, M. & Espel, E. Role of LFA-1 and ICAM-1 in Cancer. *Cancers*, 9(11), 153 (2017).

Ruella, M. & Maus, M. V. Catch me if you can: Leukemia Escape after CD19-Directed T Cell Immunotherapies. *Computational and Structural Biotechnology Journal*, 14, 357–362 (2016).

Salter, A. et al Comparative analysis of TCR and CAR signaling informs CAR designs with superior antigen sensitivity and in vivo function. *Science Signaling*, 14(697) (2021).

Sceneay, J. et al. Interferon Signaling Is Diminished with Age and Is Associated with Immune Checkpoint Blockade Efficacy in Triple-Negative Breast Cancer. *Cancer Discovery*, 9(9), 1208–1227 (2019).

Schanda, N. et al. Sensitivity and Specificity of CD19.CAR-T Cell Detection by Flow Cytometry and PCR. *Cells*, 10(11), 3208. (2021).

Slaney, C. Y., Kershaw, M. H. & Darcy, P. K. Trafficking of T Cells into Tumors. *Cancer Research*, 74(24), 7168–7174. (2014).

Stevens, A. et al. Programming multicellular assembly with synthetic cell adhesion molecules. *Nature*, 614(7946), 144–152 (2023).

Subklewe, M., Bergwelt-Baildon, M. von & Humpe, A. Chimeric Antigen Receptor T Cells: A Race to Revolutionize Cancer Therapy. *Transfusion Medicine and Hemotherapy*, 46(1), 15–24 (2019).



Teppert, K., Wang, X., Anders, K., Evaristo, C., Lock, D. & Künkele, A. Joining Forces for Cancer Treatment: From “TCR versus CAR” to “TCR and CAR.” *International Journal of Molecular Sciences*, 23(23), 14563 (2022).

Walling, B. L. & Kim, M. LFA-1 in T Cell Migration and Differentiation. *Frontiers in Immunology*, 9, 952 (2018).

Ying, Z. et al. Parallel Comparison of 4-1BB or CD28 Co-stimulated CD19-Targeted CAR-T Cells for B Cell Non-Hodgkin’s Lymphoma. *Molecular Therapy – Oncolytics*, 15, 60–68 (2019).

## **Chapter 2- Engineering synthetic adhesion molecules to program cell-cell interaction**

### **Abstract**

Cell adhesion molecules are ubiquitous in multicellular organisms, specifying precise cell-cell interactions in processes as diverse as tissue development, immune cell trafficking, and wiring of the nervous system(Honig et al.,2020;Ley et al.,2007, Sanes et al.,2020) Here, we show that a wide array of synthetic cell adhesion molecules (synCAMs) can be generated by combining orthogonal extracellular interactions with intracellular domains from native adhesion molecules, such as cadherins and integrins. The resulting molecules yield cell-cell interactions with adhesion properties similar to native interactions. The synCAM intracellular domain identity dominates in specifying interface morphology and mechanics, while diverse homotypic or heterotypic extracellular interaction domains independently specify the connectivity between cells. This toolkit of orthogonal adhesion molecules enables rationally programmed assembly of novel multicellular architectures, as well as systematic remodeling of native tissues. The modularity of synCAMs provides fundamental insights into how distinct types of cell-cell interfaces may have evolved. Overall, these tools offer powerful new capabilities for cell and tissue engineering and for systematically studying multicellular organization.

## Introduction

The ability to systematically program cell-cell adhesion would provide powerful new tools to study development, neurobiology and immunology, and could facilitate the custom design and repair of multicellular tissues and therapeutic cells (**Fig. 1a**) (Todhunter et al.,2015;Blauch et al, 2018). Nonetheless, engineering cell adhesion remains an underexplored area within the emerging field of synthetic biology.

Native cell-cell interactions are mediated by a large collection of cell adhesion molecules (CAMs) -- complex transmembrane proteins that bind to a neighboring cell or matrix and induce a mechanical adhesive response, often involving cytoskeletal and morphological rearrangements (Cavallaro et al.,2011; Rubinstein et al.,2015). Examples of CAMs include integrins, which assemble focal adhesions, and cadherins, which assemble adherens junctions between epithelial cells (Kinashi et al.,2005;Yap et al.,2003). The structural complexity and functional diversity of CAMs makes it unclear if the extracellular binding and intracellular domain-mediated cytoskeletal reorganization functions can be uncoupled and recombined to generate novel cell-cell connectivities, but prior studies indicate some potential modularity (Geiger et al., 1992;LaFlamme et al.,1994; Lilienbaum et al.,1995;Young et al., 2001;Schoenit et al., 2022).

Here we systematically explore the modularity of CAMs by fusing well-characterized orthogonal extracellular binding domains (ECD) to endogenous intracellular domains (ICDs), thereby generating synthetic CAMs (synCAMs). We characterize the synthetic cell-cell interfaces that result and test whether synCAMS can precisely program novel multicellular organization.

## RESULTS

### ***Fusing orthogonal extracellular binding domains to adhesion intracellular domains yields native-like cell-cell adhesion interactions***

We first generated heterophilic synCAMs in which a well characterized orthogonal binding interaction – the GFP/aGFP (nanobody) interaction – is fused to the ICDs of E-cadherin (Ecad), Integrin b1 (Intb1), Integrin b2 (Intb2), Intercellular Adhesion Molecule 1 (ICAM-1), Delta-like protein 1 (DLL1), Junctional adhesion molecule B (JAM-B), Neural cell adhesion molecule 1 (NCAM-1), and Mucin 4 (MUC-4) (**Fig. 2.1b**) (Fridy et al., 2014). For all synCAMs, we fused both the transmembrane region (TM) and ICD from the donor CAM to the GFP/aGFP ECD.

We tested whether cognate synCAM pairs with symmetrically matched ICDs can drive junction formation between L929 mouse fibroblasts (a cell line with low endogenous adhesion that has classically been used to assess cadherin differential adhesion sorting) (Nose et al., 1988; Foty et al., 2005). Cells expressing cognate synCAMs were mixed in a flat bottom, ultra-low attachment (ULA) plate, and the resulting pairs of adhered cells were imaged by confocal microscopy after 3 hours (**Fig. 2.1c**).

We compared the synCAM driven interfaces with those formed by native adhesion molecules (e.g., WT Ecad) or by a simple tether (GFP/aGFP fused to a transmembrane domain lacking any ICD). All synCAMs/tethers were expression matched to ensure that functional differences were not artifacts of varying surface receptor levels (**Fig. 2.6**). The GFP/aGFP synCAMs led to the formation of cell pairs, with several synCAMs (ICDs: Ecad, Intb1, Intb2, ICAM-1, MUC-4) forming extensive

interfaces comparable to those observed with native cadherin. These native-like interfaces form despite these molecules completely lacking their large native extracellular domains. In comparison, the tether (no ICD) pairs did not form extensive interfaces, showing only a small point of contact.

Several other synCAMs (ICDs: NCAM-1, JAM-B, DLL1) exhibited a distinct phenotype: resulting interfaces were small, but with significant interface enrichment of the GFP-labelled synCAMs (**Fig. 2.1c**). In contrast, the GFP signal in the tethered cell pairs is distributed throughout the entire membrane. Thus, these synCAMs seem to drive a distinct phenotype of highly focused spatial clustering at the interface when engaged.

To more quantitatively analyze interface size and enrichment for each synCAM interaction (15-20 cell pairs), we measured contact angle -- a metric of apparent cell-cell surface tension -- that is correlated with interface size (**Fig. 2.1d**). (Maitre et al., 2012; Barreiro et al., 2022). We also measured GFP-tagged synCAM interface enrichment fraction (vs non-interface GFP - **Fig. 2.1e**). These results support the general observation of two main classes of synCAM phenotypes: one class induces formation of large, extensive cell-cell interfaces (ICDs: Ecad, Intb1, Intb2, and ICAM-1, MUC-4), and another class induces formation of small but highly enriched interfaces (ICDs: NCAM-1, JAM-B, DLL1; Note: MUC-4 and ICAM-1 show both large interfaces and some degree of interface enrichment). Each of these synCAM interface classes is highly distinct from the simple tether interaction.

### ***SynCAM ICD has a dominant effect on formation of an extensive or enriched cell-cell interface compared to ECD affinity***

Both a strong extracellular domain binding interaction and intracellular domain coupling with the cytoskeleton could contribute to tight cell-cell interface formation (Maitre et al., 2012; Winklbauer et al., 2015). SynCAM modularity uniquely enables investigating the relative ECD and ICD contributions to interface formation. Using the ICAM-1 synCAM as a testbed system, we characterized cell-cell interfaces with varied ECD affinity (using a well characterized affinity series of GFP nanobodies) or deleted ICD (**Fig. 2.1f; Fig. 2.6**) (Fridy et al., 2014). Reducing the ECD affinity from a  $K_d$  of 0.7 nM to 3  $\mu$ M ( $>10^3$  fold) gradually decreases the resulting cell-cell contact angle and interface size, but even the weakest ECD exhibits a significantly expanded interface. In contrast, deletion of the ICAM-1 ICD, even in the presence of a high affinity ECD, disrupts the interface completely. A similar modest decrease of cell-cell contact angle was observed for synCAMs with an Intb1 ICD when the ECD  $K_d$  was varied between 0.7 nM to 110 nM (**Fig. 2.7**). These observations are consistent with a model in which cytomechanical changes mediated by the ICDs play a dominant role in determining the extent of interface expansion (Maitre et al., 2012; Winklbauer et al., 2015).

In addition, we characterized how decreasing ECD interaction affinity impacts the GFP enrichment phenotype observed for NCAM-1. Here, the GFP receptor remains highly enriched at the interface when ECD affinity is varied over the range of  $K_d = 0.7$  nM to 600 nM (**Fig. 2.7**). Thus, the enriched interface phenotype also appears to be driven largely by the ICD identity.

The dominance of the ICD over ECD affinity in determining adhesion properties was further corroborated in competition sorting assays (**Fig. 2.9**). Here, cells expressing two different aGFP synCAM (ICAM-1 ICD) variants compete to co-sort with GFP synCAM “bait” cells. The higher “affinity” cells are observed to preferentially sort to the center of the cell cluster with the bait cells. This complementary assay thus also indicates that the ICD primarily determines adhesion preferences while ECD affinity provides a secondary level of fine tuning. In addition, cell-cell interfaces were characterized for GFP-ICAM-1 and GFP-tether cells expressed at different levels (**Fig. 2.8**). For GFP-ICAM-1/aGFP-ICAM-1 interfaces, the contact angle correlates with the synCAM expression level. However, for the GFP-tether/aGFP-tether interfaces, the contact angles remain constant regardless of the expression level.

### ***Different synCAMs induce distinct interface cytoskeletal morphologies***

To explore the interfaces generated by synCAMs in more detail, we turned to a more controlled system in which a cell expressing an aGFP synCAM interacts with a GFP-coated surface (**Fig. 2.2, Fig. 2.10**). Here, unlike studying two interacting cells, GFP is immobile on one side of the interface and does not rearrange. As a result, interacting synCAM L929 cells spread on the surface. We plated cells on the surface and allowed them to spread over 75 minutes. Cells were then fixed and stained with phalloidin to observe the actin cytoskeleton. A simple aGFP tether interaction yielded minimal cell spreading on the GFP surface (**Fig. 2.2a**). However, cells expressing synCAMs once again exhibited two distinct modes of spreading. Cells expressing synCAMs with ICDs from ICAM-1, Integrin-beta1, Integrin-beta2, and Ecad uniformly

expanded on the GFP surface and developed a dense band of cortical actin along the periphery of the cell (**Fig. 2.2b**). Kinetic studies show that this larger cell spreading is associated with a slow phase of tens of minutes to hours, as expected if significant cytoskeletal remodeling is required (**Data Fig. 2.11**). These behaviors are consistent with uniform “expansive” spreading along the entire periphery of the cell. In contrast, synCAMs with the MUC-4, NCAM-1, and JAM-B ICDs yielded a “fried egg” morphology when spreading on the GFP surface: a smaller central cell mass was surrounded by thin membrane protrusions at the periphery (**Fig. 2.2c**). In these cases, lamellipodial and/or filopodial actin structures mediated radially “protrusive” spreading. Overall, these surface spreading studies are consistent with our prior cell-cell interface studies, as the “expansive spreading” synCAMs also lead to larger cell-cell interfaces and greater contact angles, while the “protrusive spreading” synCAMs form small but highly enriched interfaces.

We further investigated how synCAM-driven cell spreading was altered in the presence of a series of small molecule inhibitors of distinct actin regulators (**Fig. 2.12**). All synCAM expressing cells displayed minimal spreading in the presence of Latrunculin, B which disrupts actin filament formation, confirming the importance of cytoskeletal activity at all stages and modes of cell spreading. In contrast, inhibiting contractility with blebbistatin but still allowing for actin polymerization, enabled synCAM cells to spread, but without controlled assembly of actin into distinct structures unique to the different synCAMs. This result emphasizes the competition between spreading and cortical contractility as a cell extends a new interface (Winklbauer et al., 2015; Cuvelier et al., 2007). For protrusive spreading synCAMs (e.g. JAM-B ICD), the lamellipodial



sheets normally seen at the periphery of the cell appear to be disrupted by CK666, indicating a role of its target, the Arp2/3 complex, in formation of these thin protrusive structures.

The different interface morphologies observed both in the cell-cell and cell-surface context can be explained by postulated mechanisms of the CAM ICDs (**Fig. 2.2e**). Although they individually differ in detail, the expansive ICDs (Ecad, ICAM-1, integrins) recruit adapter molecules such as b-catenin, talin, vinculin, and ERM proteins, which are thought to engage the cortical actin cytoskeleton and can thus drive expansion of the entire cell front (Kinashi et al.,2005; Yap et al.,2003). In contrast, the protrusive ICD's (NCAM-1, JAM-B, DLL1) interact with PDZ scaffold proteins or lipid rafts – generally forming organized complexes that involve clustering or phase separation (Beutel et al., 2019;Sytnyk et al.,2006;Tetzlaff et al.,2018). The resulting spatially focused assemblies may then drive protrusive cytoskeletal responses such as formation of filopodia and lamellipodia (by recruiting and activating proteins like N-WASP and Arp2/3). The importance of these ICD interaction domains in interface formation was confirmed by mutational analysis of key signaling motifs (**Fig. 2.13**).

### ***Imbalanced synCAM interactions yield disrupted or asymmetric interfaces***

Many endogenous cell adhesion molecules bind homophilically (e.g., Ecad, NCAM-1, and JAM-B), yielding an interface with symmetric ICDs. However, many other endogenous cell adhesion molecules participate in heterophilic interactions (e.g., Intb1, Intb2, and ICAM-1), leading to cell-cell interfaces with different opposing ICDs. We therefore used the synCAM platform to systematically investigate how symmetric vs

asymmetric ICDs impact cell-cell interface morphology. We examined all possible pairs of different GFP/aGFP synCAMs in L929 fibroblast cells (all have GFP/aGFP ECDs; ICDs include Ecad, Intb1, Intb2, ICAM-1, MUC-4, NCAM-1, JAM-B, or no ICD). Cell pairs were mixed in a flat bottom low attachment plate and imaged after 3 hours by confocal microscopy (**Fig. 2.3, Fig. 2.14**).

Asymmetric interfaces with a fully deleted ICD on one side of the interface (i.e., “tether” on one side) exhibit significantly disrupted interfaces: they show minimal cell-cell interface expansion and contact angle increase compared to the symmetric interfaces (**Fig. 2.3a, b**). However, a large expansive interface can be formed if an asymmetric interface is composed of pairing two expansive synCAMs (e.g., Ecad:ICAM-1 or Ecad:Intb2) with contact angles of similar value to symmetric ICDs (**Fig. 2.3a, 2.3b**). These findings suggest that large, expanded interfaces can form with asymmetric synCAMs if the opposing ICD’s yield a balanced interaction (in contrast, having tether on one side disrupts formation of the expansive interface). Analogously, asymmetric interfaces with paired ICDs that mediate GFP enrichment (e.g., NCAM-1:MUC-4, NCAM-1:JAM-B) generate an interface enrichment phenotype in line with that of the symmetric interfaces (**Fig. 2.3a, 2.3b**). Thus, to form a productive interface, the exact sequence of an opposing ICD seems less critical than the presence of ICDs with similar strength and morphology.

Interestingly, when we created heterotypic interfaces in which a cell with a protrusive synCAM binds to a cell with an expansive synCAM, we found that the cells interacted with a consistent asymmetric morphology: they form a directional interface in which the protrusive synCAM cell wraps around the expansive synCAM cell (**Fig. 2.3c**).

Together these results show the rich diversity of interfaces that can be predictably constructed with different combinations of synCAM pairs.

***SynCAMs can be engineered with diverse hetero- and homotypic extracellular binding domains to program de novo multicellular assembly***

Programming the formation of novel multicellular tissues de novo is a fundamental goal in synthetic biology that requires dictating specific cellular connectivity within a multicellular system (Todhunter et al., 2015; Gatner et al., 2009; Glass et al., 2018). Prior efforts to orthogonally control multicellular assembly, both in bacteria and mammalian systems, have generally employed surface tethering to facilitate adhesion (Todhunter et al., 2015; Gatner et al., 2009; Glass et al., 2018). This goal requires dictating specific cellular connectivity within a multicellular system. Given the capability of synCAMs to direct cellular morphology and cytoskeletal structure, we next tested whether synCAMs could be engineered with a wide range of orthogonal ECDs to also rationally program specific spatial patterning. We found that functional synCAMs could be built with multiple distinct antibody-antigen binding pairs, including HA-tag/aHa scFv, maltose binding protein (MBP) /aMBP nanobody, B cell surface antigen CD19 /aCD19 scFV, tyrosine-protein kinase Met (c-Met) /ac-Met nanobody, mCherry /amCherry nanobody, and epidermal growth factor receptor (EGFR) /aEGFR nanobody (**Fig. 2.4a**). The orthogonality of these different ECD synCAMs was confirmed by co-sorting assays in L929 cells and quantified for their efficiency in excluding WT L929 cells from the multicellular assembly (**Fig. 2.15**).

We then tested whether this set of orthogonal heterotypic synCAMs could program highly specific cell “bonding” patterns. (**Fig. 2.4b**). We constructed assemblies with the following patterns: 1) two cell  $A \leftrightarrow B$  “alternating” heterophilic interactions (generated by expression of a heterophilic GFP-aGFP synCAM pair in cells “A” and “B”); 2) three cell  $A \leftrightarrow B \leftrightarrow C$  “bridging” interactions (generated by expression of orthogonal synCAMs in cells “A” and “C”, and both complementary synCAMs in the bridging cell “B”); 3) three cell  $A \leftrightarrow B \leftrightarrow C \leftrightarrow A$  “cyclic” interactions (generated by expression of two orthogonal synCAMs in each of cells “A”, “B”, and “C”). The resulting assemblies organize as precisely dictated by the synCAM-defined cell-cell connectivities. The Harmony image analysis software was used to quantitate the distribution of directly contacting cells for each cell type (**Fig. 2.4b**). This analysis showed that the synCAM engineered cell interactions dominate. In addition, as shown in the close-up images with low numbers of cells, the cyclic interaction set can lead to the predicted minimal 3 and 4 multi-cell assemblies (**Fig. 2.4b**). Thus, synCAM combinations can control the precise “bonding” connectivities between cells within a multicellular assembly.

We next engineered homotypic synCAMs from self-dimerizing coiled-coil ECD interactions. We focused on the Aph4 (computationally designed) and the IF1 (bovine ATPase inhibitor IF1) leucine zippers, as we anticipated that their antiparallel binding topologies might sterically favor intercellular trans-cell interactions over intracellular *cis* binding (Negron et al., 2014; Rhys et al., 2014). We also appended an intervening fibronectin domain (an extracellular domain from fibronectin) adjacent to both the Aph4 and IF1

coiled-coil domains to provide additional separation from the juxtamembrane region which could further favor trans cell interactions (**Fig. 2.4c**) (Jacobs et al., 2012). We tested if sets of cells expressing orthogonal homophilic synCAMs could predictably generate structures with segregated spatial compartments. Cells expressing three different orthogonal homotypic CAMs (WT Ecad, Aph4-ICAM-1, or IF1-ICAM-1) were mixed in different combinations, characterized by confocal microscopy after 48 hours (**Fig. 2.4d**), and classified by their resulting assembly structures. The individual cell populations show clear sorting as defined by their homophilic synCAMs, but most striking is the highly modular sorting behaviors that result. When cell types are mixed in a pairwise manner, we see that the IF1 cells sort to the center vs Ecad or Aph4. The Ecad and Aph4 cells sort into a two-lobed barbell structure. These relationships are maintained when all three cell types are mixed, yielding a structure with an Ecad/Aph4 barbell cell assembly with IF1 cells at the core (frequency of assembly types is shown in **Fig. 2.16**). These results show how a toolkit of orthogonal synCAMs can build complex, multi-compartment self-organizing structures with modularity and predictability.

### ***SynCAMs can drive cell intercalation into assemblies mediated by native adhesion interactions***

We also tested if synCAMs could directly interface with a tissue held together by native adhesion molecules like P-cadherin (Pcad). Thus, we engineered a synCAM with an aPcad scFv fused to the ICAM-1 ICD (**Fig. 2.4e, Fig. 2.17**). We found that these synthetic Pcad-targeting cells intercalated into a cell spheroid held together by the endogenous homophilic adhesion molecule, Pcad. In contrast, cells lacking the synCAM

were excluded and sorted to the exterior of the structure. Thus, synCAMs can integrate new cells into assemblies formed by native adhesion molecules.

***SynCAMs bind in primary and iPSC derived cells.***

We next tested whether synthetic adhesion molecules could function in other cell types, particularly in primary cells or induced pluripotent stem cell (iPSC) derived cells. GFP/ aGFP-ICAM-1 synCAMs and GFP/aGFP-tether molecules (no ICD) were expressed in several primary or iPSC-derived cells (**Fig. 2.18**). When ICAM-1 based synCAMs are expressed in primary human dermal fibroblasts, human mesenchymal stromal cells, and iPSC-derived smooth muscle cells, we observed strong localization of the GFP tagged synCAMs to the interface formed with partner cells expressing a functional cognate aGFP synCAM. This synCAM relocation to the heterotypic cell-cell interface is not observed either in unbound cells (GFP synCAM remains distributed throughout cell, not just at interface) or when co-cultured with partner cells containing only an aGFP tether (no ICD). These results demonstrate that cognate synCAMs functionally engage each other in these different cell types, and that the engagement is dependent on both cognate ECDs, and presence of a strong ICD on both sides of the interface.

### ***Remodeling tissue organization by introducing synthetic adhesion links***

We next examined whether introducing synthetic adhesion could remodel and reconfigure multicellular tissues organized by native CAMs. For example, we have previously generated WT Ecad and WT Pcad L929 cell lines that differentially sort from each other into a bilobed assembly (Toda et al.,2018). We then asked whether introduction of expansive synCAMs could overcome the sorting mediated by WT cadherins and remodel this structure to integrate the two previously separated populations. To engineer this integration, we expressed cognate GFP/aGFP synCAMs in the two cell populations containing ICDs known to yield different adhesion strengths (**Fig. 2.5a**). Expression of a heterotypic “tether” molecule converted the bilobed assembly into a two layered (“core-shell”) structure. This two-layered structure slightly increases the number of heterophilic contacts relative to the bilobed assembly, but maintains sorting mediated by the differential WT cadherins. In contrast, expression of the stronger ICAM-1 or Ecad synCAMs converted the bilobed structure into an interspersed structure in which the strong synthetic heterophilic interaction forces the two cell types into a single mixed compartment (note: the Ecad synCAM appears to have two effects: it creates strong heterophilic binding and has some dominant negative inhibitory effects on WT cadherin adhesion, likely through competition for the same pool of intracellular effectors). A similar synCAM-mediated integration could also be driven between differentially sorted L929 cell populations expressing WT Pcad or WT Ncad. Thus, synCAMs can be used to systematically remodel multi-cell assemblies.

To further explore tissue remodeling, we tested whether synCAMs could alter epithelial monolayers, a fundamental building block for diverse tissues and organs. For

example, modulation of epithelial structure by interactions with mesenchymal cells is a common theme in development. In this case we used Madin-Darby Canine Kidney (MDCK) cells as a starting epithelial cell structure. Plated by themselves, MDCK cells form a confluent epithelial layer on the plate. When a population of L929 cells expressing Pcad are added, the L929 cells form distinct homotypic spheroid clusters that sit above the MDCK epithelial layer. Thus, the starting epithelial (MDCK) and spheroid (Pcad L929) tissues show minimal interactions and function as independent assemblies (**Fig. 2.5b**).

We then asked whether introducing bridging synthetic adhesion interactions (using GFP/aGFP ECD with symmetric ICDs) would force the distinct epithelial and spheroid tissues to interact. When a minimal tether bridging interaction (no ICD) is added, the Pcad-L929 cells sit tightly upon the MDCK epithelial layer, but still act independently and maintain their initial spheroid structure. Introducing a stronger Ecad synCAM, however, results in the Pcad-L929 spheroids spreading into flatter, aster-like, bumps that more extensively contact the epithelial layer. Finally, including an ICAM-1 synCAM bridging interaction causes dramatic cooperative rearrangement of both tissues (**Fig. 2.5b, far right**). In this case, the L929 cells organize into ribbon-like assemblies and form an organized lattice-like network atop the MDCK cells (most visible in zoomed out view). Moreover, the strong bridging interaction between the L929 and MDCK cells appears to pull the MDCK cells from the surface in the intervening spaces of the lattice, forcing them into the lattice-like network. We hypothesize that this cooperative tissue emerges from the opposing of forces of the two tissues. The strong homotypic (Pcad) attraction among the L929 cells combined with the strong synthetic



bridging interaction (synCAM) between the L929 cells and the MDCK cells results in these two populations adopting a mechanically balanced state. In this new state, the epithelial cells concentrate along the links forming the lattice, closely aligned with the cords of L929 cells. The resulting network is reminiscent of the self-organizing capillary tube network of activated endothelial cells. In short, this network configuration appears to provide a solution that allows the L929 cells to simultaneously maintain a high degree of homotypic interaction, along with a high degree of interaction with the MDCK epithelial layer.

A similar emergent lattice network structure was observed when we performed an analogous experiment in primary cells. In this case we used a monolayer formed from primary mouse intestinal epithelial cells and a second layer composed of mouse embryonic fibroblast (MEF) cells. We again explored the effects of introducing a bridging synCAM interaction between the two distinct, largely non-interacting tissues. While a tethering interaction did not significantly reorganize the tissues, introduction of a strong synCAM (ICAM-1 ICD), led again to formation of MEF elongated networks. In summary, we show that synCAMs can systematically couple otherwise independent cell populations to yield novel multi-cell systems whose cooperative mechanics yield complex tissue structures.

## DISCUSSION

This work reveals the potential for engineering diverse synthetic adhesion molecules that share the design principles of native adhesion molecules, but which specify new and orthogonal physical connectivities between cells. Although metazoans deploy a plethora of cell adhesion molecules to mediate diverse cellular interactions and tissue assembly, many more novel interfaces likely remain untapped by evolution. The synCAM design strategy used here incorporates two central modes for controlling synthetic adhesion. First, the extracellular interaction domain specifies cell-cell connectivity (“bonding”), which can be either homophilic or heterophilic with precisely controlled affinity. Second, the intracellular domain dictates cytoskeletal reorganization and largely determines the interface mechanics and morphology. The orthogonality and tunability of extracellular domain recognition coupled to the modularity of intracellular domain output expands the capabilities provided by WT CAMs for use in tissue engineering. This toolkit can thus alter both cell-cell connectivity and the resulting interface type. Furthermore, mixing multiple synCAMs and native CAMs to create a system of mechanically coupled cells can generate tissues with complex emergent structures.

Lastly, because synCAMs can impart a custom ECD interaction from a small protein domain such as a nanobody or leucine zipper, they are more compact in size than WT adhesion molecules such as ICAM-1, Ecad, and NCAM-1, whose ECDs are 480, 709, and 718 amino acids respectively. This enhanced compaction increases compatibility with the size-limitations of adeno-associated virus and lentivirus delivery approaches presently applied in cell and gene therapies.

The broad spectrum of adhesion ICDs amenable to chimeric engineering demonstrates that intracellular domain function is to some degree independent of the endogenous extracellular recognition mechanism. It is noteworthy that the simple extracellular interactions utilized in this work do not match the higher regulatory sophistication of many natural ECDs, which can also show cis-oligomerization, catch bonding, and allosteric changes (Rubinstein et al., 2015; Hynes et al., 2002, Luo et al., 2006; Wu et al., 2010). Nonetheless, synCAMs are still sufficient to assemble similar cell-cell interfaces. The modularity of CAMs provides insights into how many natural CAMs may have evolved. For example, proteins with Cadherin ECDs are found in choanoflagellates (the closest single cell relatives to metazoans), but they lack the metazoan ICDs (Abedin et al., 2008; King et al., 2003). These proteins may have been used by choanoflagellates to bind food or substrates rather than for cell-cell adhesion and then later co-opted for cell-cell adhesion through recombination with intracellular signaling domains (King et al., 2003).

This work also supports a dominant role of the intracellular domain in dictating the character of CAM mediated cell-cell interfaces. Tethering interactions between cells that do not engage the cytoskeleton are unable to generate strong, extensive interfaces, no matter what the extracellular binding affinity is. In contrast, synCAMs consisting of ICDs that engage the cytoskeleton facilitate a more complex morphology that depends on the identity of the ICD on each side of the interface. These observations are consistent with prior studies that suggest that cadherin ICDs remodel cortex tension to drive cell interface expansion and resistance to cell separation (Maitre et al., 2012; Winklbauer et al., 2015).

Finally, we show that synCAMs provide a versatile toolkit for programming novel multicellular structures, either de novo or by intercalating or remodeling tissues formed by native CAMs. The toolkit of synCAMs also enables systematic perturbation of self-organizing systems that could be used to analyze the mechanism of diverse developmental processes. In the future, these types of engineered adhesion molecules could potentially be applied to address therapeutic problems that employ native adhesion molecules, such as to precisely direct tissue repair and regeneration or to control the interactions and trafficking of immune and neural cells.

## REFERENCES

Honig, B. & Shapiro, L. Adhesion Protein Structure, Molecular Affinities, and Principles of Cell-Cell Recognition. *Cell* 181, 520–535 (2020).

Ley, K., Laudanna, C., Cybulsky, M. I. & Nourshargh, S. Getting to the site of Inflammation: the leukocyte adhesion cascade updated. *Nat. Rev. Immunol.* 7, 678–689 (2007).

Sanes, J. R. & Zipursky, S. L. Synaptic specificity, recognition molecules, and assembly of neural circuits. *Cell* 181, 536–556 (2020). Todhunter, M. E. et al. Programmed synthesis of three-dimensional tissues. *Nat. Methods* 12, 975–981 (2015).

Toda, S., Blauch, L. R., Tang, S. K. Y., Morsut, L. & Lim, W. A. Programming self-organizing multicellular structures with synthetic cell-cell signaling. *Science* 361, 156–162 (2018). Cavallaro, U. & Dejana, E. Adhesion molecule signalling: not always a sticky business. *Nat. Rev. Mol. Cell Biol.* 12, 189–197 (2011).

Rubinstein, R. et al. Molecular logic of neuronal self-recognition through protocadherin domain interactions. *Cell* 163, 629–642 (2015).

Tsai, T. Y.-C., Garner, R. M. & Megason, S. G. Adhesion-Based Self-Organization in Tissue Patterning. *Annu. Rev. Cell Dev. Biol.* (2022)

Kinashi, T. Intracellular signalling controlling integrin activation in lymphocytes. *Nat. Rev. Immunol.* 5, 546–559 (2005).

Yap, A. S. & Kovacs, E. M. Direct cadherin-activated cell signaling: a view from the plasma membrane. *J. Cell Biol.* 160, 11–16 (2003)

Geiger, B., Salomon, D., Takeichi, M. & Hynes, R. O. A chimeric N-cadherin/beta 1-integrin receptor which localizes to both cell-cell and cell-matrix adhesions. *J. Cell Sci.* 103 ( Pt 4), 943–951 (1992).

LaFlamme, S. E., Thomas, L. A., Yamada, S. S. & Yamada, K. M. Single subunit chimeric integrins as mimics and inhibitors of endogenous integrin functions in receptor localization, cell spreading and migration, and matrix assembly. *J. Cell Biol.* 126, 1287–1298 (1994)

Lilienbaum, A., Reszka, A. A., Horwitz, A. F. & Holt, C. E. Chimeric integrins expressed in retinal ganglion cells impair process outgrowth in vivo. *Mol. Cell. Neurosci.* 6, 139–152 (1995).

Young, B. A. et al. The cytoplasmic domain of the integrin alpha9 subunit requires the adaptor protein paxillin to inhibit cell spreading but promotes cell migration in a paxillin-independent manner. *Mol. Biol. Cell* 12, 3214–3225 (2001)

Schoenit, A. et al. Tuning Epithelial Cell-Cell Adhesion and Collective Dynamics with Functional DNA-E-Cadherin Hybrid Linkers. *Nano Lett.* 22, 302–310 (2022).

Fridy, P. C. et al. A robust pipeline for rapid production of versatile nanobody repertoires. *Nat. Methods* 11, 1253–1260 (2014).

Nose, A., Nagafuchi, A. & Takeichi, M. Expressed recombinant cadherins mediate cell sorting in model systems. *Cell* 54, 993–1001 (1988).

Foty, R. A. & Steinberg, M. S. The differential adhesion hypothesis: a direct evaluation. *Dev. Biol.* 278, 255–263 (2005).

Maître, J.-L. et al. Adhesion functions in cell sorting by mechanically coupling the cortices of adhering cells. *Science* 338, 253–256 (2012).

Winklbauer, R. Cell adhesion strength from cortical tension - an integration of concepts. *J. Cell Sci.* 128, 3687–3693 (2015).

Cuvelier, D. et al. The universal dynamics of cell spreading. *Curr. Biol.* 17, 694–699 (2007).

Barreiro, O. et al. Dynamic interaction of VCAM-1 and ICAM-1 with moesin and ezrin in a novel endothelial docking structure for adherent leukocytes. *J. Cell Biol.* 157, 1233–1245 (2002).

Beutel, O., Maraspini, R., Pombo-García, K., Martin-Lemaitre, C. & Honigsmann, A. Phase separation of zonula occludens proteins drives formation of tight junctions. *Cell* 179, 923-936.e11 (2019).

Sytnyk, V., Leshchyn'ska, I., Nikonenko, A. G. & Schachner, M. NCAM promotes assembly and activity-dependent remodeling of the postsynaptic signaling complex. *J. Cell Biol.* 174, 1071–1085 (2006).

Tetzlaff, F. et al. MPDZ promotes DLL4-induced Notch signaling during angiogenesis. *eLife* 7, (2018).

Gartner, Z. J. & Bertozzi, C. R. Programmed assembly of 3-dimensional microtissues with defined cellular connectivity. *Proc Natl Acad Sci USA* 106, 4606–4610 (2009).

Glass, D. S. & Riedel-Kruse, I. H. A Synthetic Bacterial Cell-Cell Adhesion Toolbox for Programming Multicellular Morphologies and Patterns. *Cell* 174, 649-658.e16 (2018).



Negron, C. & Keating, A. E. A set of computationally designed orthogonal antiparallel homodimers that expands the synthetic coiled-coil toolkit. *J. Am. Chem. Soc.* 136, 16544–16556 (2014).

Rhys, G. G. et al. Maintaining and breaking symmetry in homomeric coiled-coil assemblies. *Nat. Commun.* 9, 4132 (2018).

Jacobs, S. A. et al. Design of novel FN3 domains with high stability by a consensus sequence approach. *Protein Eng. Des. Sel.* 25, 107–117 (2012).

Hynes, R. O. Integrins: bidirectional, allosteric signaling machines. *Cell* 110, 673–687 (2002).

Luo, B.-H. & Springer, T. A. Integrin structures and conformational signaling. *Curr. Opin. Cell Biol.* 18, 579–586 (2006).

Wu, Y. et al. Cooperativity between trans and cis interactions in cadherin-mediated junction formation. *Proc Natl Acad Sci USA* 107, 17592–17597 (2010).

Abedin, M. & King, N. The premetazoan ancestry of cadherins. *Science* 319, 946–948 (2008).

King, N., Hittinger, C. T. & Carroll, S. B. Evolution of key cell signaling and adhesion protein families predates animal origins. *Science* 301, 361–363 (2003).

Guan, X. M., Kobilka, T. S. & Kobilka, B. K. Enhancement of membrane insertion and function in a type IIIb membrane protein following introduction of a cleavable signal peptide. *J. Biol. Chem.* 267, 21995–21998 (1992).

UniProt Consortium. UniProt: the universal protein knowledgebase in 2021. *Nucleic Acids Res.* 49, D480–D489 (2021).

Zimmermann, I. et al. Synthetic single domain antibodies for the conformational trapping of membrane proteins. *eLife* 7, (2018).

Zhao, N. et al. A genetically encoded probe for imaging nascent and mature HA-tagged proteins in vivo. *Nat. Commun.* 10, 2947 (2019).

Grupp, S. A. et al. Chimeric antigen receptor-modified T cells for acute lymphoid leukemia. *N. Engl. J. Med.* 368, 1509–1518 (2013).

Roovers, R. C. et al. A biparatopic anti-EGFR nanobody efficiently inhibits solid tumour growth. *Int. J. Cancer* 129, 2013–2024 (2011).

- Williams, J. Z. et al. Precise T cell recognition programs designed by transcriptionally linking multiple receptors. *Science* 370, 1099–1104 (2020).
- Mahe, M. M. et al. Establishment of gastrointestinal epithelial organoids. *Curr. Protoc. Mouse Biol.* 3, 217–240 (2013).
- Andersson-Rolf, A., Fink, J., Mustata, R. C. & Koo, B.-K. A video protocol of retroviral infection in primary intestinal organoid culture. *J. Vis. Exp.* e51765 (2014)
- Thorne, C. A. et al. Enteroid monolayers reveal an autonomous WNT and BMP circuit controlling intestinal epithelial growth and organization. *Dev. Cell* 44, 624-633.e4 (2018).
- Celli, L., Ryckewaert, J.-J., Delachanal, E. & Duperray, A. Evidence of a functional role for interaction between ICAM-1 and nonmuscle alpha-actinins in leukocyte diapedesis. *J. Immunol.* 177, 4113–4121 (2006).
- Anthi, N. J. et al. The structure of an integrin/talin complex reveals the basis of inside-out signal transduction. *EMBO J.* 28, 3623–3632 (2009). García-Alvarez, B. et al. Structural determinants of integrin recognition by talin. *Mol. Cell* 11, 49–58 (2003).

Huber, A. H. & Weis, W. I. The structure of the beta-catenin/E-cadherin complex and the molecular basis of diverse ligand recognition by beta-catenin. *Cell* 105, 391–402 (2001).

Little, E. B., Edelman, G. M. & Cunningham, B. A. Palmitoylation of the cytoplasmic domain of the neural cell adhesion molecule N-CAM serves as an anchor to cellular membranes. *Cell Adhes. Commun.* 6, 415–430 (1998).

## Methods

### *Materials*

Oligonucleotides were purchased from Integrated DNA Technologies (Coralville, IA). In-Fusion cloning reagent, CloneAmp HiFi PCR Premix, Lenti-X™ concentrator kit, and Stellar chemically competent cells were purchased Takara Bio (Kusatsu, Shiga, Japan). Miniprep kits and spin columns were purchased from Qiagen (Hilden, German). FuGENE® HD Transfection Reagent was purchased from Promega (Madison, WI). DMEM, GlutaMAX™, Alexa Fluor 647 Phalloidin (A22287) and Alexa Fluor 555 Phalloidin (A34055) were purchased from Thermo Fisher Scientific (Waltham, MA). Fetal bovine serum (FBS) was purchased from the University of California, San Francisco [UCSF] Cell Culture Facility. L929 mouse fibroblast cells (ATCC# CCL-1) were purchased from the American Type Culture Collection (Manassas, VA). Madin-Darby Canine Kidney (MDCK) cells were a gift from the Mostov Lab at UCSF. Primary dermal fibroblast cells (CC-2511), mouse embryonic fibroblast cells (M-FB-481), and human bone marrow derived mesenchymal stem cells (PT-2501) were purchased from Lonza Bioscience (Basel, CH). Nexcelom 3D 384-well ultra-low attachment treated round bottom multi-well plates were purchased from Nexcelom Bioscience (Lawrence, MA). Cellstar® Cell-Repellent Surface 384-Well flat bottom plates were purchased from Greiner Bio-One (Frickenhausn, DE). 384 Well Optical Imaging Flat Clear Bottom TC-Treated plates were purchased from Corning Inc (Corning, NY). H9 hPSCs (WA09) were purchased from WiCell (Madison, WI). EDTA (46-034-CI) and growth factor-reduced Matrigel (356231) were purchased from Corning (Corning, NY). Geltrex,

hESC-qualified (A1413302), Essential 8 Flex Medium Kit (A2858501), Essential 6 Flex Medium Kit (A1516401), and Advanced DMEM/F12 (12634028) were purchased from Thermo Fisher Scientific (Waltham, MA). Recombinant Human/Mouse/Rat Activin A protein (338-AC-050) was purchased from R&D Systems (Minneapolis, MN). FBS for iPSCs- (#1701) was purchased from ScienCell (Carlsbad, CA). CellMask™ deep red plasma membrane dye was purchased from Invitrogen (Waltham, MA). Phalloidin-iFluor 405 Reagent (ab176752) was purchased from Abcam (Cambridge, United Kingdom).

The following antibodies were purchased and diluted in PBS prior to use per the manufacturer's protocol:

- 1.DYKDDDDK Tag (D6W5B) Rabbit mAb (Binds to same epitope as Sigma's Anti-FLAG® M2 Antibody) (Alexa Fluor® 647 Conjugate) #15009 Cell signaling technology
- 2.DYKDDDDK Tag (D6W5B) Rabbit mAb (Binds to same epitope as Sigma's Anti-FLAG® M2 Antibody) (Alexa Fluor® 488 Conjugate)
- 3.Myc-Tag (9B11) Mouse mAb (Alexa Fluor® 647 Conjugate) Cell signaling technology
- 4.EGFR Antibody (DH8.3) [Alexa Fluor® 647] Novus bio

### ***Equipment***

Cell sorting and flow cytometry was carried out using FACSAria II Cell Sorter or LSR II Flow Cytometer (Beckton-Dickinson). Confocal microscopy was carried out on an Opera Phenix automated spinning disk confocal microscope with 20x water-immersion objective in 384 well plates, a Nikon TiE with CSU-X1 spinning disk confocal unit: 60x and 100x oil immersion objectives, or a Zeiss LSM 980 with Airyscan 2, 40x water immersion objective.

### ***Synthetic adhesion receptor construct design and cloning***

All constructs were cloned into a pHR vector containing the SFFV promoter, Kozak consensus sequence, and cleavable signal sequence of influenza hemagglutinin (MKTIIALSYIFCLVFA).

To design the constructs, the transmembrane and intracellular regions from cellular adhesion molecules were identified from topology annotations in UniProt (Uniprot Consortium et al., 20120). Codon optimized genes encoding each CAM ICD and TM region were purchased from Integrated DNA Technologies (Coralville, IA) and inserted into the vector using In-Fusion cloning. Each CAM TM and ICD region was fused to an extracellular binding domain (e.g., GFP,  $\alpha$ GFP) using In-Fusion cloning (see supplementary sequence list). Sequences for all nanobody or scFv ECDs were obtained from previously reported work or from publicly available patents (Zimmermann et al., 2018; Zhao et al., 2019; Grupp et al., 2019; Roovers et al., 2011; Williams et al., 2020). For the experiments involving intestinal epithelial cells, an internal ribosome entry site (IRES) and a puromycin-N-acetyltransferase gene (Puro) were cloned downstream of the GFP-ICAM-1 and GFP-Tether constructs within the pHR vector. Plasmids were sequence verified by RF Biotech (Hayward, CA).

### ***Lentivirus***

Lentivirus was generated by cotransfecting vectors encoding packaging proteins (pMD2.G and p8.91) with pHR plasmid of interested using the Fugene 6 HD transfection reagent (per manufacturer's protocol) in HEK293-T cells plated in 6-well plates at

approximately 70% confluence. Two days after transfection, viral supernatants were collected, passed through a 0.45 mm filter and used immediately for transduction. For transduction of primary cells, lentivirus was concentrated 20-fold using the Lenti-X™ Concentrator kit (Takara) and following the manufacturer's protocol.

### ***Cell Lines***

L929 and MDCK cells were cultured in DMEM containing 10% FBS. To generate stable cell lines, viral supernatant (50-400 µL) was diluted with 1.5 mL of media and plated directly with cells ( $1 \times 10^5$  L929 or MDCK) in 12-well dishes. 24 hr post-infection, the viral media was replaced with normal growth media and the cells were expanded into a T25 flask. The cells were stained for the appropriate epitope tag with a fluorescently tagged antibody and sorted for expression by FACS. Unless otherwise noted, a bulk-sorted population was used for each experiment. To generate the GFP-ICAM-1 and GFP-Tether L929 cell lines with tuned expression level, total virus added to the cells was titrated between 50 and 400 µL, and the cells were sorted for different synCAM expression levels by FACS. For the Aph4 and IF1 synCAMs, single-cell populations were established by sorting individual cells into a 96-well plate.

### ***Antibody Staining and Flow Cytometry Analysis***

To confirm the expression level of synCAMs in each cell line, the cells were analyzed by FACS. The cells were detached with TrypLE and transferred to a round-bottom 96- well plate. The cells were pelleted by centrifugation (4 min, 400 g), the supernatant was removed, and the cells were resuspended in 40 µL PBS containing a



fluorescent-dye conjugated antibody. Cells were stained for 50 minutes at 4°C. The cells were then washed twice with PBS and resuspended in PBS with 5% FBS. The cells were then analyzed by flow cytometry (BD LSR II). The flow cytometry data was then analyzed in FlowJo (TreeStar).

### ***Contact angle and receptor enrichment measurements for cell-cell pairs***

Prior to carrying out the experiment, all cell lines were detached using TrypLE, resuspended in 1 mL DMEM, counted, and then diluted to  $4 \times 10^5$  cells/mL. L929 cells stably expressing cytosolic BFP and a GFP synCAM were mixed 1:1 with L929 cells expressing cytosolic mCherry and an aGFP synCAM in a 384 well cell-repellent surface flat bottom plate ( $3.2 \times 10^4$  cells, 80  $\mu$ L total volume, 37 °C). At  $t = 3$  hr, the plates were imaged at 20X magnification by fluorescence confocal microscopy (Phenix). Maximum projection images were exported from the manufacturer's software (Harmony). Cell pairs of similar size were identified, and contact angles were measured in FIJI (ImageJ). The GFP enrichment percentage was determined in FIJI by measuring the GFP signal localized at the cell-cell interface as a fraction of that present in the entire cell. Data analysis for the measured contact angle and enrichment values was carried out in Prism 9 (Graphpad).

### ***Cell spreading experiments***

We characterized the rate, interface size, and morphology of spreading synCAM cells on a GFP-coated surface. Purified GFP protein was diluted to a final concentration of 0.5  $\mu\text{M}$  in PBS and enough volume applied ( $\sim 100\mu\text{L}$ ) to coat the bottom surface of an 8-well glass bottomed imaging chamber. This solution was incubated for 10 minutes on ice. Excess solution was removed and the chamber rinsed with PBS. Next, the chamber was blocked with a solution of 10 mg/mL Bovine Serum Albumin (BSA) and 1mg/mL Beta Casein (Sigma) for a minimum of 1 hour on ice. The blocking solution was removed and the chamber washed 3 times with PBS. When using CellVis (C8-1.5H-N) chambers, an anti-6x-His antibody (ab18184) and 6x-His-tagged GFP (ab134853) were used to obtain full coverage of the surface with GFP. A 100x dilution of antibody in PBS was incubated on the surface of the chamber for 1 hour at 4 degrees. After being washed 3 times with PBS, a 10  $\mu\text{g}/\text{mL}$  solution containing His-tagged GFP was incubated on the surface for 1 hour at 4 degrees cel. Next, the chamber was blocked with a solution of 10 mg/mL Bovine Serum Albumin (BSA) and 1 mg/mL Beta Casein (Sigma) for a minimum of 1 hour on ice. The blocking solution was removed and the chamber washed 3 times with PBS.

To prepare the cells for the spreading assay, L929 cells were detached using Trypsin EDTA and resuspended in cell culture media.  $\sim 50\ \mu\text{L}$  of resuspended cell solution from a confluent T25 flask was added to 200  $\mu\text{L}$  of cell culture media and placed into the imaging chamber. The chamber was then transferred to a spinning disk confocal microscope equipped with an Oko Labs environmental control stage. Cells were imaged with a 60x oil immersion objective every 3 minutes over a period of 2

hours. In the first 60-90 minutes, cell spreading onto the surface was observed by monitoring cytoplasmic fluorescent proteins expressed in the cytoplasm of the synCAM cells.

Images were analyzed by binarizing the intensity to obtain a mask of the cell, which could then be used to calculate the total spread area ( $A$ ) and perimeter ( $p$ ) of the footprint. To characterize the morphology of the interface, circularity ( $c = p^2/4\pi A$ ) was calculated and compared between different synCAMs. These measurements were also made using an anti-flag tag fluorescent antibody (labels synCAM constructs) to measure area and morphology directly at the interface with the coverslip. To compare different spreading kinetics, the change in area over time was fitted with the following form:  $A = b t^{1/4}$  where  $b$  is the spreading rate coefficient. This model was previously used to compare the kinetics of spreading cells on an adhesive surface.<sup>21</sup> Analysis was implemented in MatLab (2020a).

### ***Immunostaining***

To visualize the actin cytoskeleton, spreading cells were fixed and stained for immunohistochemistry following standard procedures. Cells were fixed in 4% PFA in cytoskeleton buffer (10 mM PIPES, 100mM NaCl, 300mM Sucrose, 1mM EGTA, 1mM  $MgCl_2$ ) for 20 minutes on ice. Cells were then washed 3 times and permeabilized with 0.1% triton X solution in PBS for 10 minutes on ice and again washed 3 times. Cells were then blocked with 10% BSA in PBS (PBS-BSA) for a minimum of 1 hour at 4 degrees. To visualize the actin cytoskeleton, cells were stained with fluorescently labelled phalloidin (conjugated with either 647, 555 or 405 fluorescent dyes). Cells were

then imaged with a spinning disk confocal microscope using a 100x magnification objective. Cell peripheries were determined by staining with CellMask™ deep red plasma membrane stain (Invitrogen). For measurements investigating the effects of cytoskeletal inhibitors on cell spreading, cells were introduced into media containing the inhibitor and allowed to spread on the GFP coated surface (CK666 100μM, Latrunculin B 5μM, SMIFH2 100μM, Blebbistatin 50μM, inhibitors were purchased from Abcam). Cells were then fixed and stained with the above procedure before being imaged with a Zeiss 980 Airyscan microscope and a 40x water immersion objective.

### ***Differential sorting assay***

Prior to carrying out the experiment, all cell lines were detached using TrypLE, resuspended in 1 mL DMEM, counted, and then diluted to  $1 \times 10^3$  cells/mL. L929 cells stably expressing cytosolic BFP and an aGFP synCAM of varying affinity were mixed 1:1:1 with L929 cells expressing cytosolic mCherry and an aGFP synCAM of varying affinity, and L929 cells expressing GFP-ICAM-1 in a 384 well ultra-low attachment (ULA) round bottom well (80 μL total volume). At  $t = 24$  hr, the wells were imaged at 20X magnification by fluorescence confocal microscopy (Phenix).

### ***Quantification of sorting assay***

To quantify the organization of different synCAM expressing cells in the multicellular differential sorting assay, we calculated the radial distribution function  $g(r)$  from multichannel 3D confocal stacks. Cells expressing mCherry and BFP were imaged at 20X magnification with a z-step size of 10 μm. Each slice in the image stack was

thresholded and binarized for each color channel, and the center of mass (COM) of the cluster found.  $g(r)$  was found by calculating the distance of each pixel from the COM and normalizing against the density of pixels within the cluster. To create a single value that captures the distribution of cells in the cluster we calculated the COM of the  $g(r)$  distribution and subtracted this value for the mCherry cells from the value for the BFP cells. Large values therefore indicate that mCherry cells are closer to the center of the cluster and small values indicate that BFP cells are closer to the center of the cluster. Image analysis was implemented in MatLab (2020a).

### ***Characterization of cell lines expressing orthogonal synCAMs***

L929 cells stably expressing synCAMs with orthogonal heterophilic pairs and a cytosolic mCherry or BFP were generated. Prior to carrying out the experiment, cell lines were detached using TrypLE, resuspending in 1 mL DMEM, counted, and then diluted to  $4 \times 10^5$  cells/mL. Each pair was mixed 1:1 in a 384 well cell-repellent surface flat bottom plate ( $3.2 \times 10^4$  cells, 80  $\mu$ L total volume, 37 °C). At  $t = 3$  hr, the plates were imaged at 20X magnification by fluorescence confocal microscopy (Phenix). Maximum projection images were generated using the manufacturer's software.

To validate the orthogonality of the heterophilic synCAM pairs, a subset was characterized for the ability to differentially sort from parental L929 cells. The synCAM cell lines were detached using TrypLE, resuspending in 1 mL DMEM, counted, and then diluted to  $1 \times 10^3$  cells/mL. Parental L929 cells were detached using TrypLE, stained with far red cell trace following the manufacturer's instructions, and diluted to  $1 \times 10^3$  cells/mL. Two synCAMs and the WT L929 cells were mixed 1:1:1 (80  $\mu$ L total) in a ULA

round bottom well and imaged after 24 hours at 20X magnification by fluorescence confocal microscopy (Phenix). Maximum projection images were then generated using the manufacturer's software (Harmony). Within the software, individual cells were segmented, and the center of the assembly was calculated based on the average position of all cells. The distance of the WT (far red) L929 cells and synCAM (BFP) cells from previously calculated center of the assembly was then determined. The difference between the average distance of WT and synCAM cells was then calculated and represented as a heat map, with greater distances corresponding to increased exclusion of WT cells from the assembly.

### ***Design and characterization of cell lines expressing homotypic synCAMs***

Homotypic synCAMs were designed to sterically impair ECD cis-interactions of the binding region. Antiparallel leucine zippers, which should favor *trans* over *cis* binding, were fused to a fibronectin linker domain, which extends the receptor from the juxtamembrane region (Negron et al.,2014; Rhys et al.,2018; Jacobs et al.,2012). Efforts to design homotypic synCAMs without the fibronectin linker were unsuccessful. These engineered ECDs were fused to an ICAM-1 TM/ICD. L929 cells stably expressing the homophilic synCAM receptors and cytosolic mCherry were generated. Clonal cell lines were obtained through single cell sorting. The cell lines were detached using TrypLE, resuspending in 1 mL DMEM, counted, and then diluted to  $1 \times 10^3$  cells/mL. The cells were incubated in a 384 well ULA round bottom plate (80 cells, 80  $\mu$ L total volume, 37 °C) for 24 hours and then imaged by fluorescence confocal

microscopy (Phenix). Maximum projection images were generated in the manufacturer's software (Harmony).

### ***Targeting endogenous Pcad***

L929 cells expressing WT Pcad and cytosolic mCherry were previously generated (Toda et al.,2018). L929 cells expressing cytosolic BFP with or without stable expression of an aPCAD synCAM (ICAM-1 TM/ICD) were mixed 1:1 with L929 cells stably expressing WT Pcad and cytosolic mCherry in a 384 well ULA round bottom plate (80 cells, 80  $\mu$ L total volume, 37 °C) for 24 hours and imaged by fluorescence confocal microscopy (Phenix). Maximum projection images were generated in the manufacturer's software (Harmony). Within the Harmony software, the total area encompassed by both the L929 cells expressing WT Pcad (mCherry) and the WT or aPcad cells (BFP) was calculated for each maximum projection image at each timepoint. The ratio of area for BFP to mCherry cells was then calculated and plotted over 24 hours, with an increased ratio corresponding to exclusion of BFP cells from the multicellular assembly (**Fig. 2.17b**). In addition, for  $t = 24$  hr, the cells were segmented and the position of the center of the assembly was calculated as the average position of the mCherry+ and BFP+ cells. The relative distance of the BFP+ and mCherry+ cells to the center of the assembly was then calculated (**Fig. 2.17c**) with a greater distance corresponding to increased exclusion of BFP+ L929 cells.

### ***Custom multicellular architecture***

For the multicellular patterning experiments, L929 cell lines were detached using TrypLE, resuspending in 1 mL DMEM, counted, and then diluted to  $1 \times 10^3$  cells/mL. Prior to dilution, the Aph4 and IF1 synCAMs were stained with far red and CFSE cell trace respectively (per manufacturer's protocol).

### ***Heterotypic assemblies***

To generate the two-cell alternating pattern, L929 cells expressing GFP-ICAM-1 (cell 1) were mixed with L929 cells expressing cytosolic mCherry, LaG16-ICAM-1 (cell 2) (1:1 80  $\mu$ L total). To generate the 3-cell bridging pattern, L929 cells expressing GFP-Ecad (cell 1) were mixed with cells expressing cytosolic mCherry, LaG16-Ecad,  $\alpha$ CD19-ICAM-1 (cell 2), and cells expressing cytosolic BFP, CD19-ICAM-1 (cell 3) (1:2:1 80  $\mu$ L total). To generate the 3-cell cyclic pattern, L929 cells expressing GFP-Ecad,  $\alpha$ MBP-ICAM-1 (cell 1) were mixed with cells expressing LaG16-ECAD, mCherry-ICAM-1 (cell 2), and cells expressing MBP-ICAM-1, LaM4-ICAM-1, cytosolic BFP (cell 3) (1:1:1 80  $\mu$ L total). In all cases, the cells were plated in ULA round bottom wells and imaged after 2 hours by confocal microscopy (Phenix). Maximum projection images were generated using the manufacturer's software (Harmony). To calculate the interaction probability tables, the cells were segmented in Harmony for each maximum projection image. Cell-cell contacts were identified from the positions of the segmented cells, and the probability for each interaction was calculated and represented as a heat map.

To form the isolated 3 cell and 4 cell cyclic assemblies, L929 cells expressing GFP-Ecad,  $\alpha$ MBP-ICAM-1 (cell 1); LaG16-ECAD, mCherry-ICAM-1 (cell 2); and MBP-



ICAM-1, LaM4-ICAM-1, cytosolic BFP (cell 3) were diluted to  $4 \times 10^3$  cells/mL and plated in a cell-repellent surface flat bottom well. Individual pairs were identified, and maximum projection images were generated and exported.

### ***Homotypic assemblies***

L929 cells expressing Wt Ecad and cytosolic BFP, Aph4-ICAM-1, or IF1-ICAM-1 were mixed with each other (either individually or all three together) in ULA round bottom wells (1:1 or 1:1:1, 80  $\mu$ L total). The cells were imaged after 48 hours by confocal microscopy. The maximum projections were generated using manufacturer's software and classified based on assembly phenotype.

### ***Primary Cell Culture***

Adult human dermal fibroblast (NHDF-Ad) and mouse embryonic fibroblast (MEF) cells were cultured in DMEM containing 10% FBS. Mesenchymal stem cells (MSCs) were cultured in Mesenchymal Stem Cell Growth Medium (Lonza). To generate stable cells expressing the synCAM constructs, viral supernatant (15  $\mu$ L of 20x concentrated virus) was diluted with 1.5 mL of media and plated directly with cells grown to 80% confluency ( $5 \times 10^4$  MSC, MEFs or NHDF plated in a 12 well dish). 24 hr post-transduction, the viral media was replaced with normal growth media and the cells were expanded into a 6 well dish. MEFs were further sorted for expression of synCAM constructs by FACS.

### ***iPSC derived cells Smooth Muscle Cells***

Human pluripotent stem cells (hPSCs) (WA09, WiCell) were maintained in E8 media on geltrex coated 6-well plates. Two days prior to initializing smooth muscle differentiation, hPSCs were dissociated with EDTA and replated into a geltrex coated 6-well plate. Once hPSCS reached confluency, E8 media was aspirated and replaced with 1mL per well of Essential 6 with 100ng/mL Activin A. The following day, the media was aspirated and replaced with 2mL per well of E6 media with 10 ng/mL BMP4. Two days later the media was aspirated and replaced with 2 mL per well of E6 media with 10 ng/mL BMP4. For days 5-9, cells were maintained with fresh E6 media + 2% FBS every other day. From day 10 onward, the media was replaced 3 times per week with Advanced DMEM/F12 + 10% FBS.

To generate SMCs with stable expression of synCAMs, the SMCs were grown to 80% confluency in a 96 well plate and transduced with 1  $\mu$ L of 20x concentrated virus. After 24 hours, the media was removed and replaced with fresh media.

### ***Mouse intestinal epithelial cells***

Intestinal epithelium was isolated and cultured as previously described(Mahe et al.,2013). Briefly, small intestinal crypts were dissociated from the duodenum of C57BL/6 mice between 6-12 weeks of age. The tissue in ice-cold PBS with 15mM EDTA for 30 minutes, then vortexed vigorously in multiple fractions to release crypts. The supernatant containing crypts was filtered on a 70  $\mu$ M mesh, and then crypts were pelleted and resuspended in growth factor-reduced Matrigel and cultured as 3D enteroids with ENR media [Advanced DMEM/F12 (Thermo Fisher 12634-028) with 1x

N2 (Thermo Fisher 17502-048), 1x B27 (Thermo Fisher 17504-044), 10 mM HEPES (Thermo Fisher 15630080), 1x GlutaMAX (Thermo Fisher 35050-061), 1 mM N-acetylcysteine (Sigma Aldrich A9165), 100 U/mL penicillin, and 100 mg/mL streptomycin (Corning 30-002), supplemented with 50 ng/mL EGF (Sigma Aldrich E9644-.2MG), 100 ng/mL Noggin (R&D 6057-NG/CF), and 5% R-spondin-conditioned media]. Media was changed every 3 days and organoids were mechanically dissociated and passaged weekly. For expression of synCAM constructs, organoids were transduced with Lentivirus as previously described (Andersson-Rolf et al.,2014). First, 3D enteroids were dissociated into single cells using TrypLe, which are then grown in growth factor-reduced Matrigel and transduction media [ NR media supplemented with 50% Wnt3a-conditioned media, 10uM Nicotinamide (Sigma Aldrich N3376-100G), 5uM CHIR (Sigma Aldrich SML1046-5MG), and 10uM Y-27632 (Sigma Aldrich Y0503-1MG)] for 3-5 days to enrich for stem cells. Enteroids were then dissociated, pelleted, resuspended in transduction media containing 8ug/ml polybrene (Sigma Aldrich H9268-5G) and concentrated lentivirus, centrifuged at 600g for 1 hour at 32°C, then incubated at 37°C for 6 hours. Cells are then pelleted and resuspended in Matrigel and grown in transduction media for 3 days, then switched to ENR media. After amplification, antibiotic selection was performed by adding 1ug/mL Puromycin (Thermo Fisher A1113803) to the media.

### ***Primary cell-cell adhesion assays***

GFP-ICAM-1, GFP-tether, aGFP-Fibcon-ICAM-1 or aGFP-Fibcon-Tether were transduced in MSCs, NHDFs, or SMCs. For these experiments, a fibcon linker domain was included for both the aGFP-ICAM-1 and aGFP-tether constructs to improve expression in primary cells. All GFP-expressing cells were co-transduced with a plasmid for expression of cytosolic BFP, and all aGFP expressing cells were co-transduced with a construct expressing cytosolic mCherry. 24 hours following transduction, the media was removed and replaced with fresh media. After 4 to 7 days, the MSCs, SMCs, or NHDFs were detached with TrypLE, resuspended in media, and plated in a 384 well plate. 24 hours after plating, the wells were imaged by fluorescence confocal microscopy (Phenix).

### ***Modifying 3D architecture***

L929 cells stably expressing WT P-cadherin, cytosolic mCherry, and LaG16-synCAM (ICAM-1, Ecad, or Tether control) were mixed 1:1 with L929 cells stably expressing WT E-cadherin, cytosolic BFP, and a GFP-synCAM (ICAM-1, Ecad, or tether control) in a ULA round bottom plate (80 total cells, 80  $\mu$ L, 24 hr, 37 °C). Prior to mixing, the L929 cell lines were detached using TrypLE, resuspending in 1 mL DMEM, counted, and then diluted to  $1 \times 10^3$  cells/mL. The assemblies were imaged by fluorescence confocal microscopy (Phenix, 20X magnification), and maximum projection images were generated in the manufacturer's software and are shown. To modify the assembly between L929 cells expressing WT Ncad and L929 cells expressing WT

Pcad, the experiment was carried out exactly as above with L929 cells expressing WT Ncad and cytosolic GFP in place of the WT Ecad cells.

### ***Modifying 2D layering***

An adherent layer of MDCK cells expressing cytosolic BFP and GFP-Tether, GFP-ICAM-1, or GFP-Ecad was formed within wells of a 384 well plate (16,000 cells plated per well). After 48 hours, L929 cells expressing WT PCAD, cytosolic mCherry, and LaG16-ICAM-1, LaG16-tether, LaG16-Ecad, or no additional receptor were added (24,000 cells per well). The interaction between the two layers was imaged by fluorescence confocal microscopy (Phenix) for 24 hours. The zoomed-out images of the assemblies were formed by stitching together nine adjacent fields of view after exporting the images from the manufacturer's software. Both the roundness and surface area of the mCherry+ assembly was quantified for each field of the experiment within the manufacturer's software (Harmony).

### ***Modifying 2D layering on intestinal epithelial organoids***

Monolayer enteroid cultures were established as previously described (Thorne et al., 2018). 3D Enteroids were dissociated into single cells using TrypLE, washed in PBS, and stained with CellTrace. 150000 cells expressing either GFP-ICAM-1 or GFP-Tether were plated onto a 384-well plate pre-coated with 5% growth factor-reduced Matrigel in 40uL ENR media supplemented with 3uM CHIR and 10uM Y-27632. After 4 hours, an additional 60uL of ENR media was added to each well. 24 hours after plating the enteroid monolayers, mouse embryonic fibroblast cells (MEFs) expressing aGFP-

Fibcon-Tether or aGFP-Fibcon-ICAM-1 and cytosolic mCherry were added (16,000 cells). After 24 hours, the wells were imaged by fluorescence confocal microscopy (Phenix). Maximum projection and 3D images were exported from the manufacturer's software (Harmony).

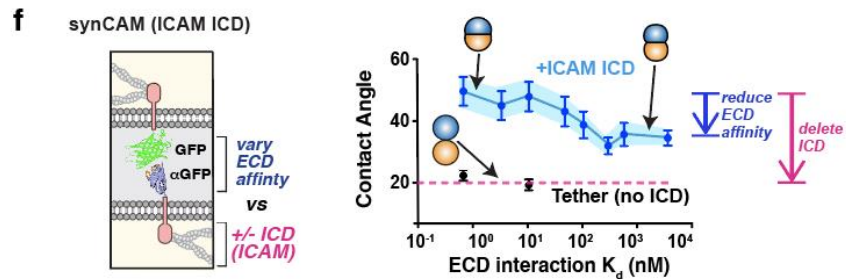
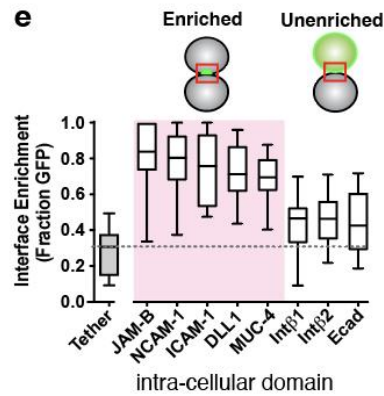
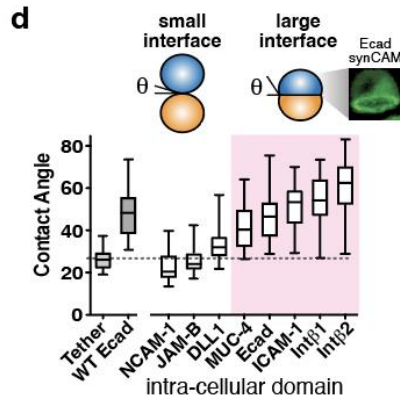
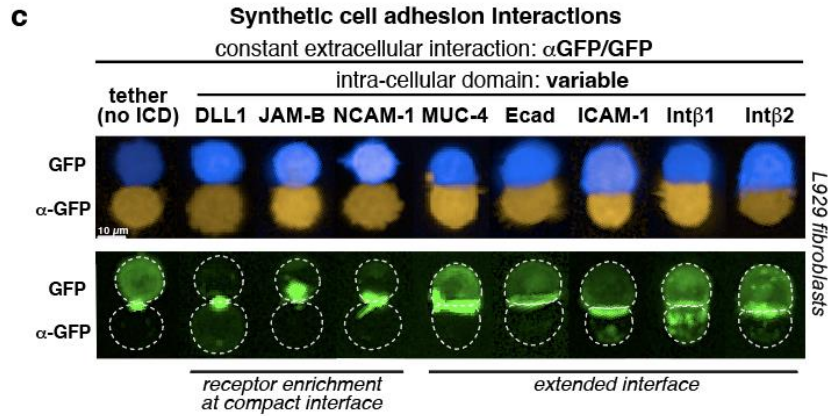
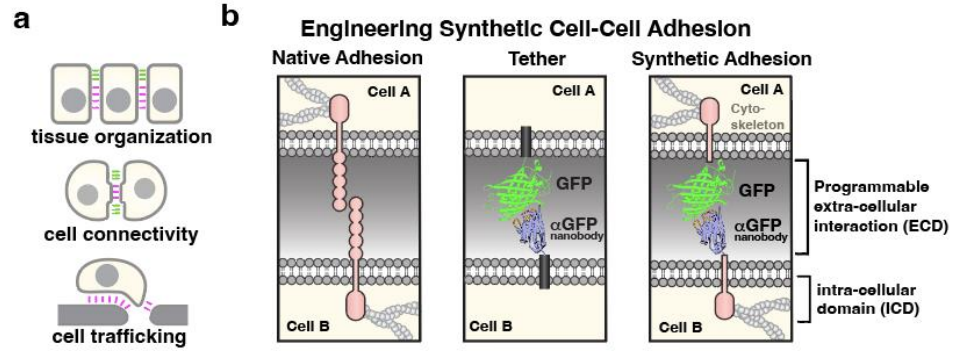


## Figure 2.1. Synthetic cell adhesion molecules (synCAMs) facilitate custom cell-cell interactions

**(a)** Potential applications to control multicellular organization and function using synthetic cell adhesion. **(b)** Conceptual design of synCAM receptors. The extracellular domain of a CAM (left) is replaced by GFP and a GFP-binding nanobody (aGFP, right). A “tether” control lacking an ICD is also shown (middle). **(c)** Top: Maximum projection of 20X confocal microscopy images of pairwise synCAM interfaces ( $t = 3$  hr): GFP-expressing cell (blue) is bound to an aGFP expressing cell (orange). The CAM TM and ICD domain for each pair is indicated (tether = control lacking ICD, DLL1 = Delta-like Protein 1, JAM-B = Junction Adhesion Molecule B, NCAM-1 = Neural Cell Adhesion molecule 1, MUC-4 = Mucin 4, ICAM-1 = Intercellular Adhesion Molecule 1, Ecad = E-cadherin, Intb1 = beta 1 integrin, Intb2 = beta 2 integrin). Bottom: GFP channel of the interfaces above highlighting differences of receptor enrichment at the interface. See **Fig. 2.6** for matched synCAM expression levels. **(d)** Box and whisker plots of contact angles measured from the interfaces shown in **a** ( $n = 15-20$  pairs). In addition, contact angles for wild type Ecad (WT Ecad) homotypic cell-cell interaction are shown. **(e)** Box and whisker plots of fraction GFP enrichment at the cell-cell interface from **c** are shown ( $n = 15-20$  pairs). **(f)** Quantification of contact angles from pairwise L929 cells expressing GFP/aGFP synCAMs with the indicated affinities and presence (blue) or absence (black) of an ICAM-1 ICD ( $n=20$  pairs,  $t = 3$  hr). See **Fig. 2.6** for matched synCAM expression levels. See **Fig. 2.9** for alternative analysis (competition cell sorting assay) of the same series of altered affinity synCAM cells.



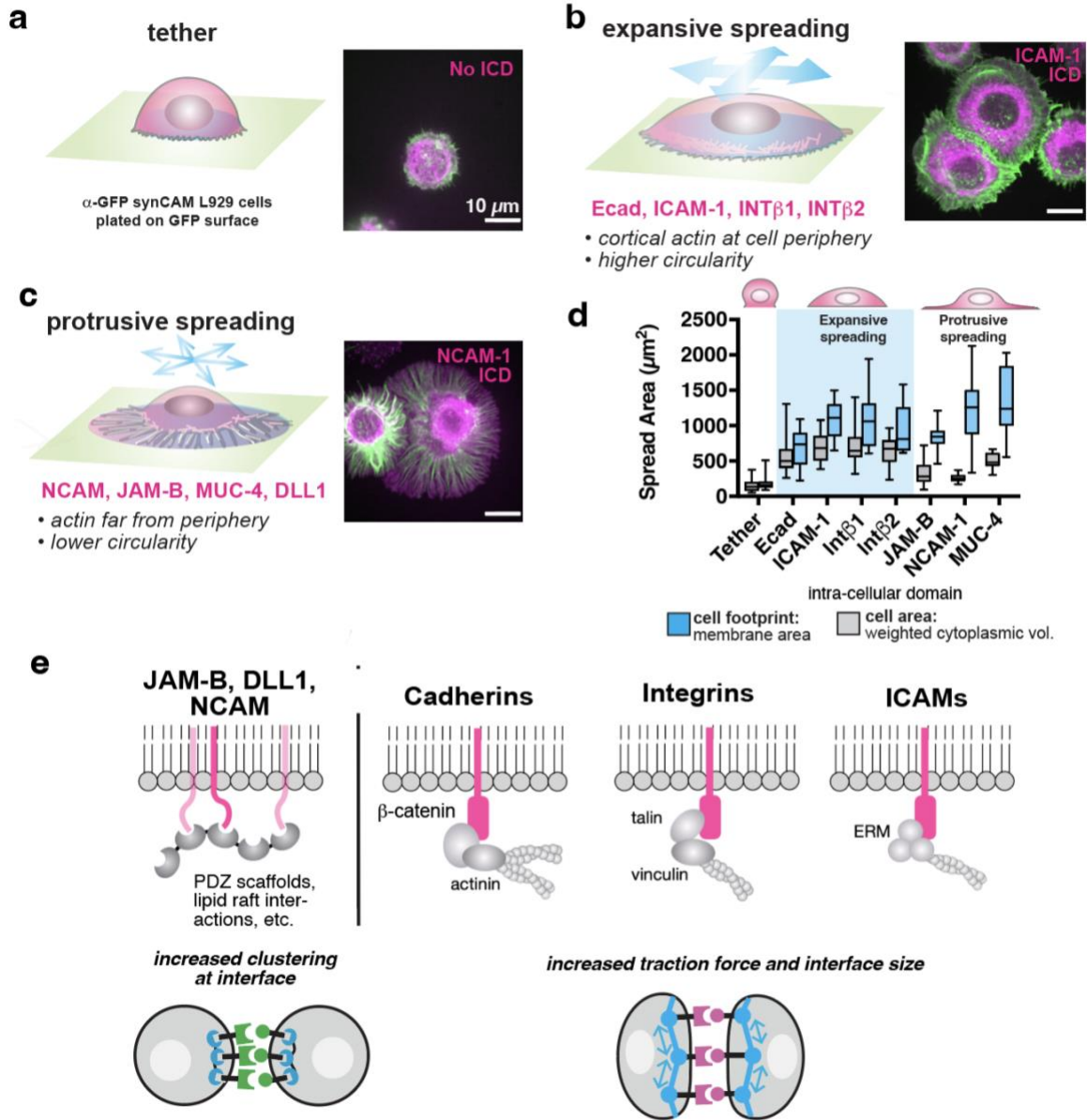


## **Figure 2.2. SynCAM intracellular domains yield distinct mechanical and morphological properties**

**(a-c)** Representative phalloidin-stained images of L929 cells expressing the indicated synCAMs spreading on a GFP-coated surface ( $t = 2\text{hr}$ ). Actin (phalloidin stain) is shown in green; full footprint of cell (membrane label) is outlined in purple. All images are shown at the same scale. **(a)** L929 cell expressing aGFP tether (no ICD) shows minimal spreading). **(b)** L929 cells expressing synCAMs with ICDs from Ecad, ICAM-1, Integrin b1, Integrin b2 show expansive spreading phenotype – cell spreads in circular manner with cortical actin at the periphery of the cell footprint. See spreading kinetic assays in **Fig. 2.11**. **(c)** L929 cells expressing synCAMs with ICDs from NCAM-1, JAM-B, and MUC-4 show protrusive spreading phenotype (a.k.a “fried egg” shape) – cortical actin does not spread very far, but cell membrane footprint extends in very thin layer beyond in bulk of cell, often with less circularity (i.e. more filopodial or lamellopodial nature). **(d)** Box and whiskers plot of the full footprint of the cell (blue) and cell area (gray) for synCAM-mediated cell spreading ( $n = 12-24$ ). **(e)** Depiction of known recruitment interactions of downstream intracellular proteins found in cell adhesion molecule ICDs. See mutational analysis of ICD binding motifs in **Fig. 2.13**

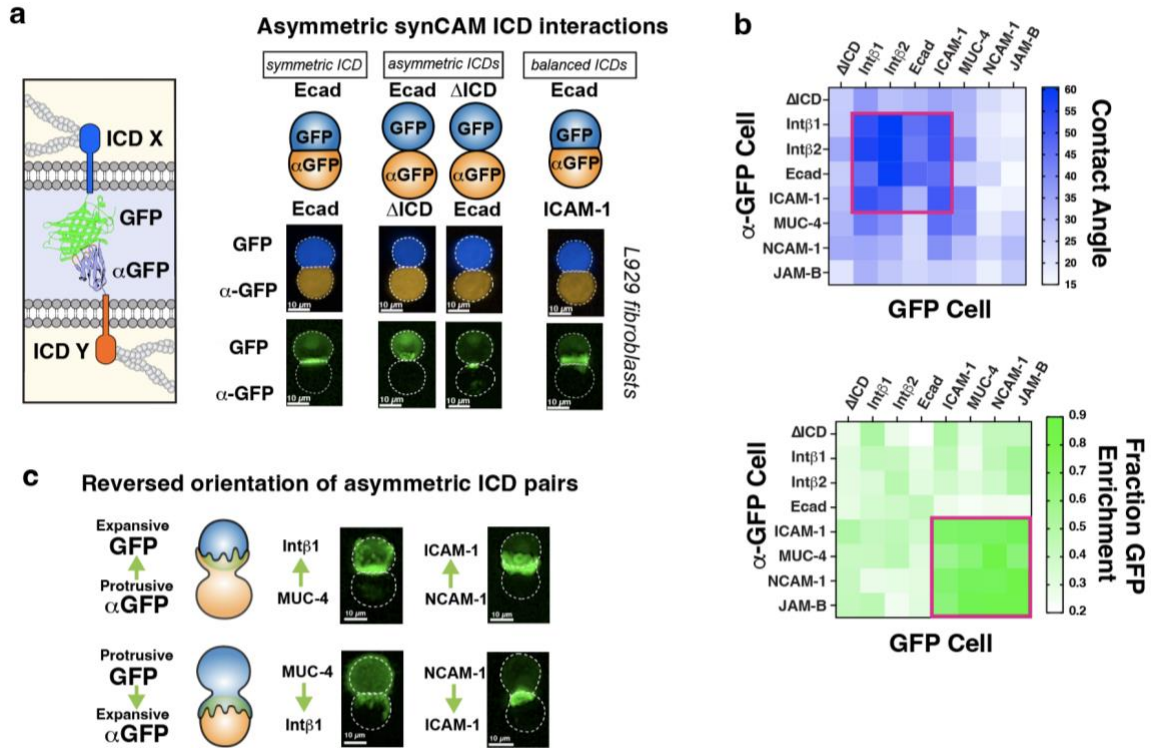
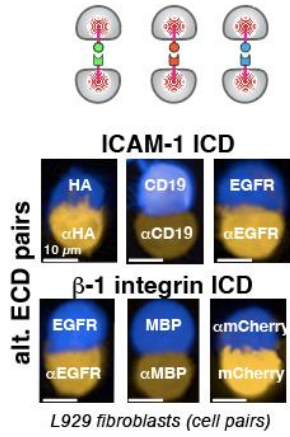


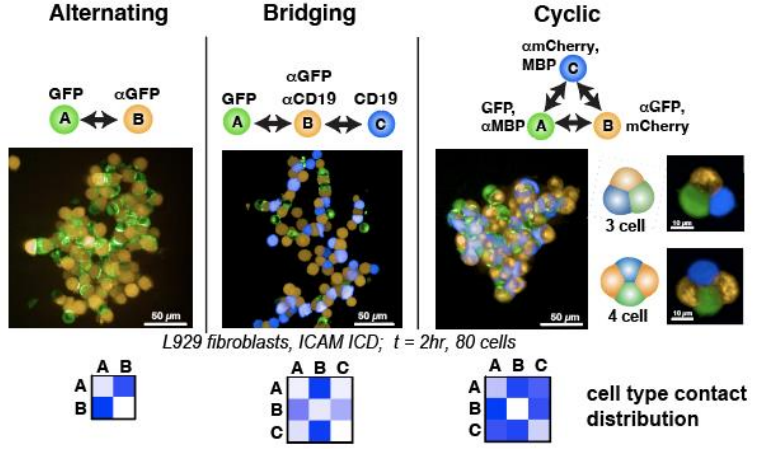
**Figure 2.3: The balance of ICD properties determines asymmetric synCAM interface morphology**

**(a)** Maximum projection of 20X confocal microscopy images of pairwise synCAM interfaces ( $t = 3$  hr) showing symmetric Ecad ICDs (left), asymmetric Ecad and Tether ( $\Delta$ ICD) interfaces (middle), and balanced asymmetric Ecad and ICAM-1 interfaces (right). The mCherry and BFP channels (top) and the GFP channels (bottom) are shown. **(b)** Quantification of contact angle (top) and GFP enrichment (bottom) for pairwise asymmetric synCAM interfaces ( $n = 10$ ). The combination of interfaces that exhibit the greatest contact angle or enrichment are outlined in red. **(c)** Example 20X confocal microscopy images of pairwise unbalanced asymmetric interfaces in which a cell expressing a protrusive synCAM binds a cell expressing an expansive synCAM. Top: Protrusive synCAM is the ICD of the aGFP-synCAM and expansive is the ICD of GFP-synCAM. Bottom: Protrusive synCAM is the ICD of the GFP-synCAM and expansive is the ICD of aGFP-synCAM.

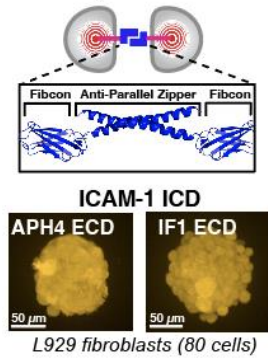
**a Orthogonal Heterophilic synCAMs**



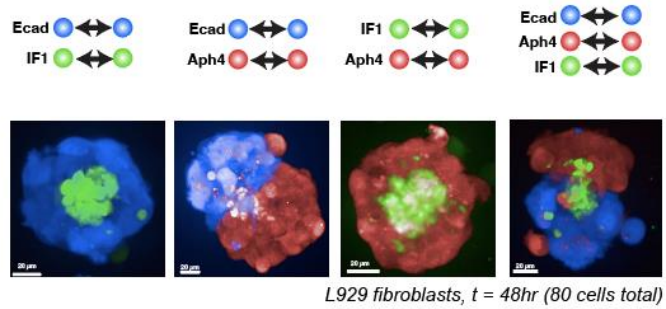
**b Custom heterotypic architectures**



**c Orthogonal Homophilic synCAMs**



**d Custom homotypic synCAM architectures**



**e Targeting Endogenous CAMs:  $\alpha$ Pcad synCAM**

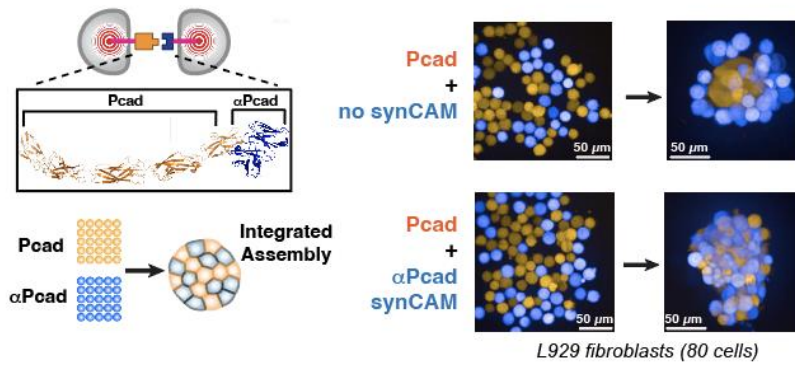


## **Figure 2.4. Programming custom multicellular assemblies with homotypic and heterotypic synCAMs**

**(a)** Heterophilic synCAMs with orthogonal extracellular recognition domains. Maximum projection of 20X confocal microscopy cell-cell interface images are shown of L929 cells expressing synCAMs with the indicated antibody-antigen pair ECDs and either ICAM-1 (top) or beta 1 integrin (bottom) TM/ICDs (t = 3hr). See **Fig. 2.15** for experimental testing of orthogonal sorting.

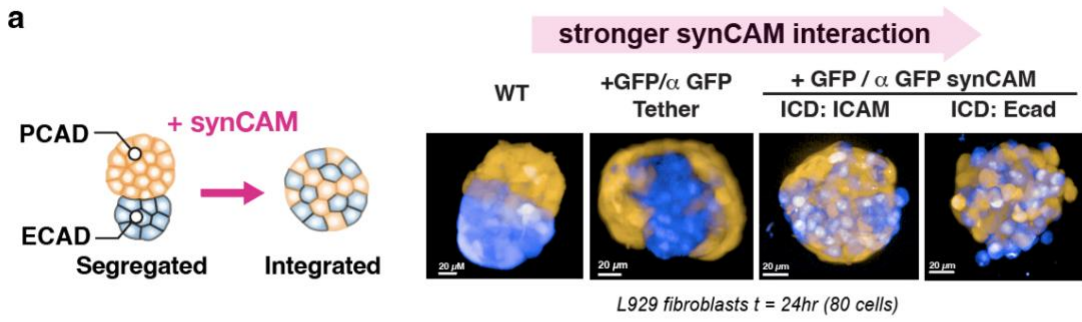
**(b)** Engineering custom heterotypic assemblies. Maximum projection of 20X confocal microscopy images of L929 cells expressing synCAMs with the indicated ECD recognition partners (t = 2hr). Assemblies form alternating “A-B” (left), bridging “A-B-C” (middle), and cyclic “A-B-C” (right) patterning. Example images of isolated cyclic interactions (t = 2 hr) are shown. Probability boxes of cell contact distribution are shown below (n = 5)

**(c)** Top: synCAM design with a homophilic binding leucine zipper ECD. Bottom: Maximum projection of 20X confocal microscopy images of L929 cells expressing homophilic binding synCAMs with the Aph4 or IF1 leucine zippers ECD and ICAM-1 TM/ICDs (ULA round bottom well, 80 cells total, t = 24 hr).

**(d)** 20X confocal microscopy images of differential sorting between L929 cells expressing WT Ecad or the indicated homophilic-binding synCAMs (t = 48 hr).

**(e)** Left: cartoon depicting the receptor design and differential sorting assay of L929 cells expressing WT P-cadherin (WT Pcad, orange) and an aPcad synCAM (aPcad, blue). The aPcad synCAM contains an ICAM-1 TM/ICD. Right: maximum projection images of the sorting assay in which L929 cells expressing WT Pcad (orange) are mixed with parental (top) or synCAM (bottom) L929 cells (blue, t=0, 24 hr).





**b**  
Mechanically coupling distinct tissues (spheroid + epithelium) via synCAM interactions

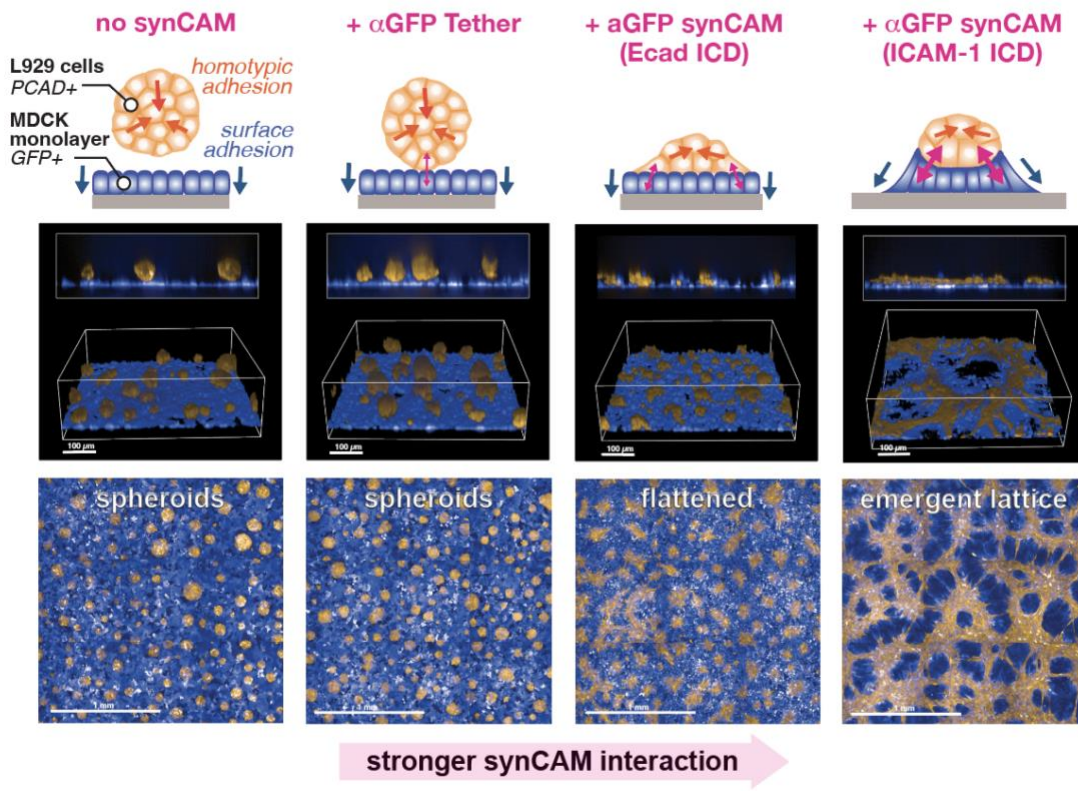


### **Figure 2.5. Using synCAMs to reshape tissue organization**

**(a)** Use of synCAMs to force integration of differentially sorting L929 populations. We start with L929 populations expressing WT Ecad (blue) or WT Pcad (orange), which leads to segregation into a binodal structure. Image shows how sorting is altered by expression of integrating heterophilic synCAM interactions of different strengths (vs tether receptor that contains a GFP/aGFP ECD, ICAM-1 TM, and  $\Delta$ ICD). Maximum projections of 20X confocal microscopy images are shown (t = 24 hr).

**(b)** L929 cells expressing WT Pcad (orange) mixed with an MDCK monolayer (blue) form spheroids that passively sit above the MDCK epithelial layer. Adding GFP/aGFP synCAM interactions of increasing strength (vs tether receptor) leads to increasing mechanical coupling between the epithelial and spheroid tissues. When strong enough, the two cell types form a complex lattice like network (ICAM-1 synCAM). Images show assembly at t = 24 hr. Both 3D zoomed in (top) and maximum projection zoomed out (bottom) views are shown.

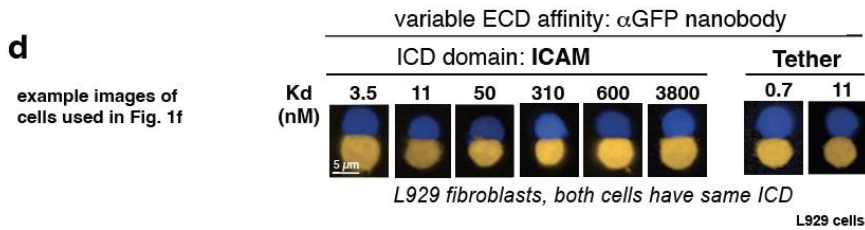
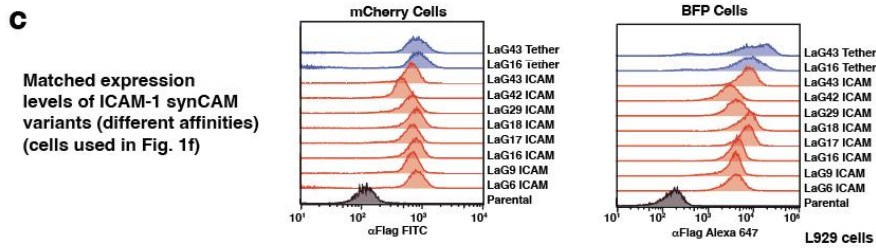
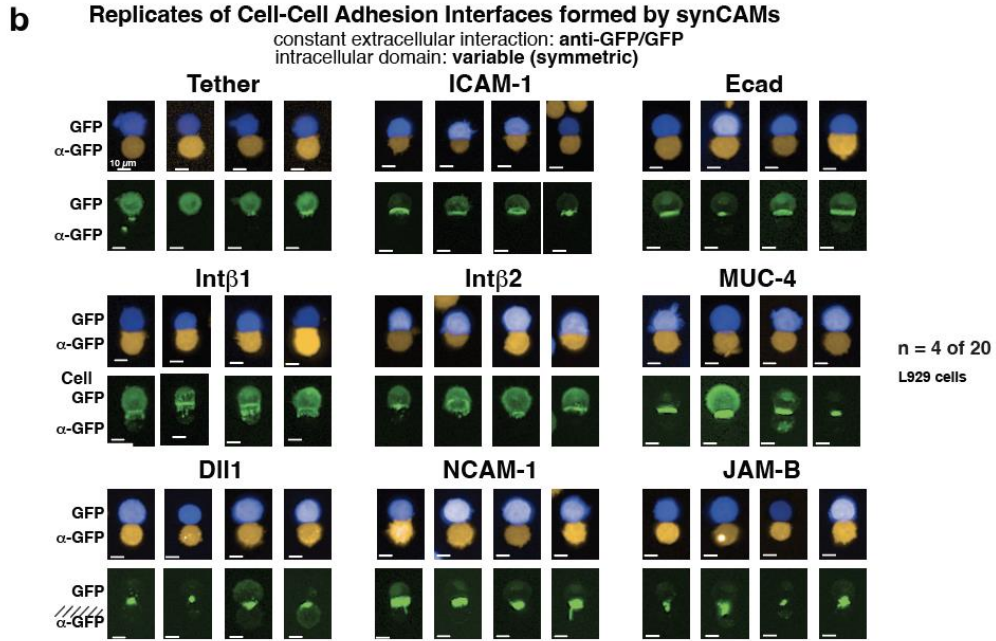
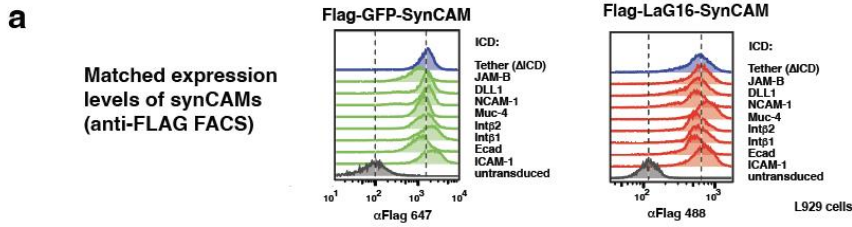




## Figure 2.6. Characterization of synCAM expression and function in L929 fibroblast cells

**(a)** FACS analysis of GFP (left) and  $\alpha$ GFP (right) synCAM expression in L929 fibroblast cells following cell sorting. Surface expression of each synCAM is measured using labelled anti-FLAG tag antibody. The CAM TM and ICD domain for each construct is indicated (tether = control lacking ICD, DLL1 = Delta-like Protein 1, JAM-B = Junction Adhesion Molecule B, NCAM-1 = Neural Cell Adhesion molecule 1, MUC-4 = Mucin 4, ICAM-1 = Intercellular Adhesion Molecule 1, Ecad = E-cadherin, Intb1 = beta 1 integrin, Intb2 = beta 2 integrin). Analysis shows that surface expression levels of the tether and alternative synCAM constructs are well matched.

**(b)** Additional replicates of synCAM cell-cell adhesion interface analysis. Maximum projection of 20x confocal microscopy images of pairwise synCAM interfaces ( $t = 3$  hr): GFP-expressing cell (blue) is bound to an  $\alpha$ GFP expressing cell (orange). The GFP channel of the interfaces is shown, highlighting differences of receptor enrichment. Four out of twenty additional examples are shown here.

**(c)** FACS analysis of  $\alpha$ GFP synCAM expression in L929 fibroblast cells expressing cytosolic mCherry (left) or BFP (right) following cell sorting. The CAM TM and ICD domain for each construct is ICAM-1, and the GFP-binding llama nanobody (LaG) ECD for each construct is indicated. This analysis shows that this series of alternative affinity synCAMs are expressed at comparable levels.

**(d)** Maximum projection of 20X confocal microscopy images of pairwise synCAM interfaces ( $t = 3$  hr): GFP-expressing cell (blue) is bound to an  $\alpha$ GFP expressing cell with the indicated binding  $K_d$  (orange).

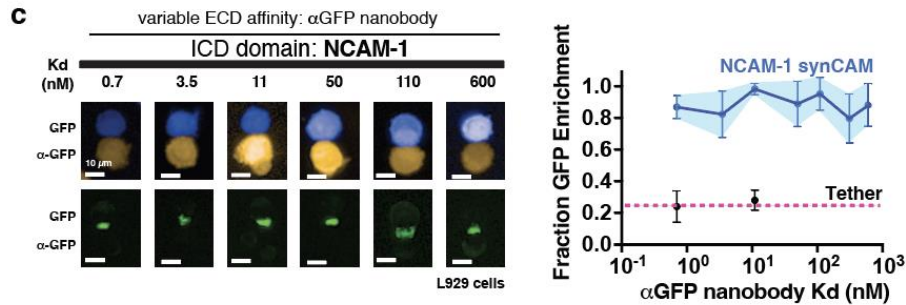
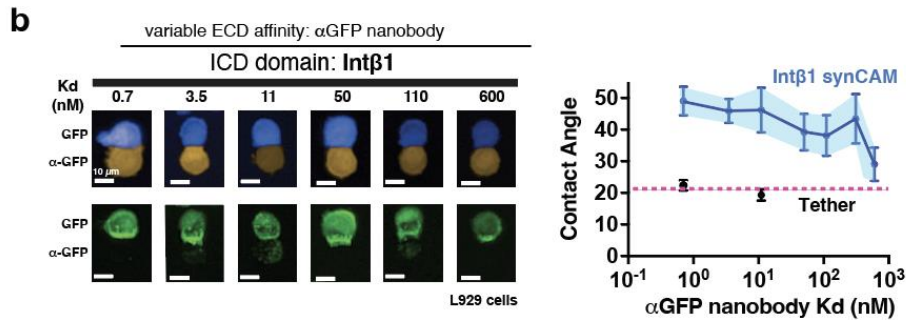
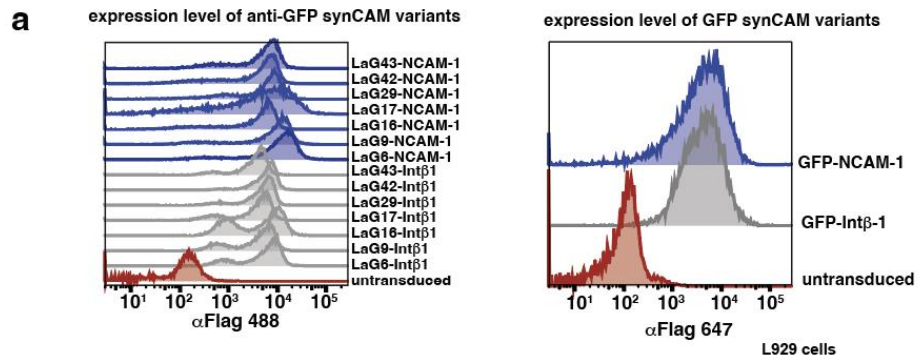


**Figure 2.7. Characterization of NCAM-1 and Intb1 synCAM function across a series of affinities.**

**(a)** FACS analysis of  $\alpha$ GFP synCAM expression in L929 fibroblast cells expressing cytosolic mCherry following cell sorting. The CAM TM and ICD domain for each construct is NCAM-1 or Intb1, and the GFP-binding llama nanobody (LaG) ECD for each construct is indicated. This analysis shows that this series of alternative affinity synCAMs are expressed at comparable levels.

**(b)** Left: Maximum projection of 20X confocal microscopy images of pairwise synCAM interfaces ( $t = 3$  hr): GFP-expressing cell (blue) is bound to an aGFP expressing cell (orange). The CAM TM and ICD domain for each pair is Intb1. Bottom: GFP channel of the interfaces above highlighting differences of receptor enrichment at the interface. Right: Plots of contact angles measured from the interfaces shown in **b** in relation to the corresponding LaG nanobody affinity ( $n = 10$  pairs error = 95 % CI). The contact angles for Intb1 (blue) are shown in relation to the tether control from **Fig. 1f** (black).

**(c)** Left: Maximum projection of 20X confocal microscopy images of pairwise synCAM interfaces ( $t = 3$  hr): GFP-expressing cell (blue) is bound to an aGFP expressing cell (orange). The CAM TM and ICD domain for each pair is NCAM-1. Bottom: GFP channel of the interfaces above highlighting differences of receptor enrichment at the interface. Right: Plots of GFP enrichment measured from the interfaces shown in **c** in relation to the corresponding LaG nanobody affinity ( $n = 10$  pairs error = 95 % CI). The GFP enrichment for NCAM-1 are shown compared to the tether control from **Fig. 1f**.

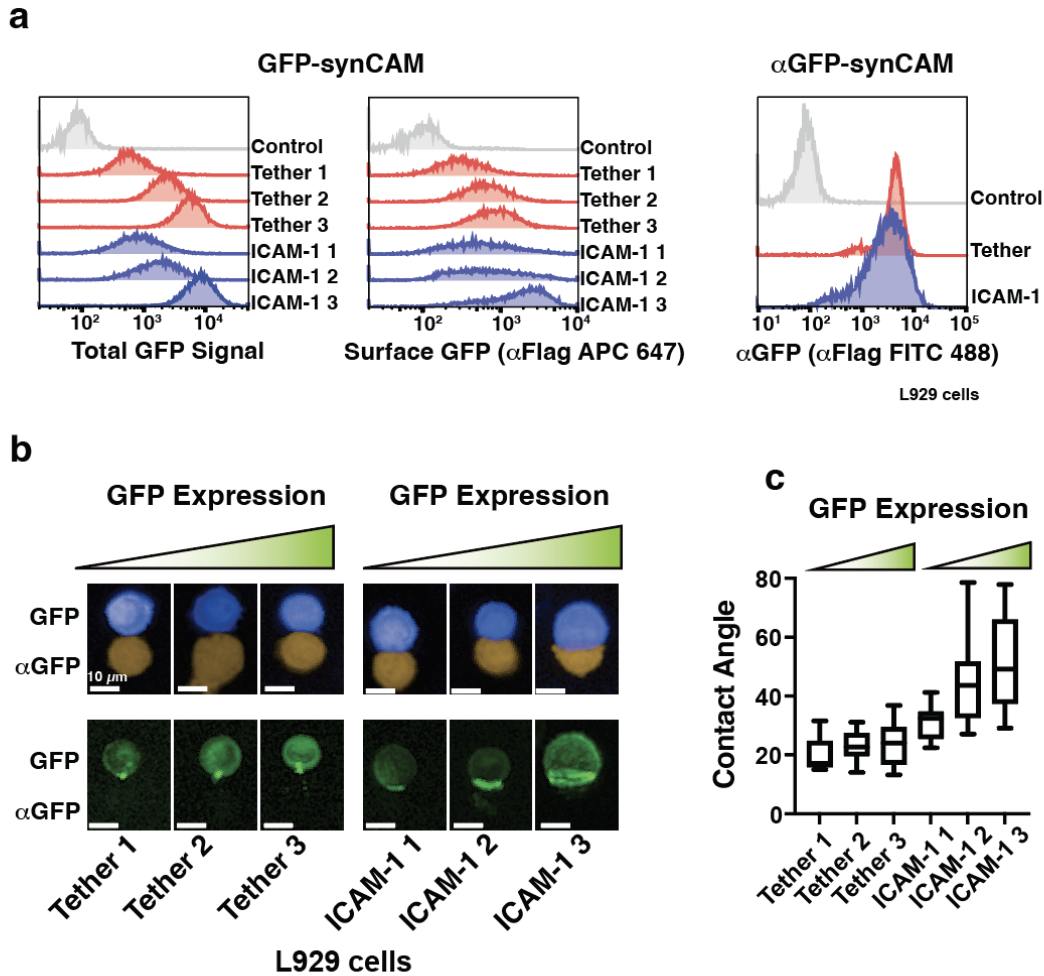
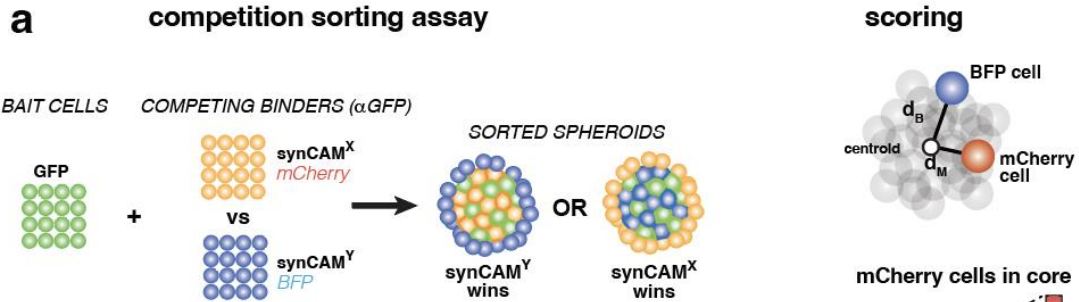


**Fig. 2.8 Characterization of tuning synCAM expression**

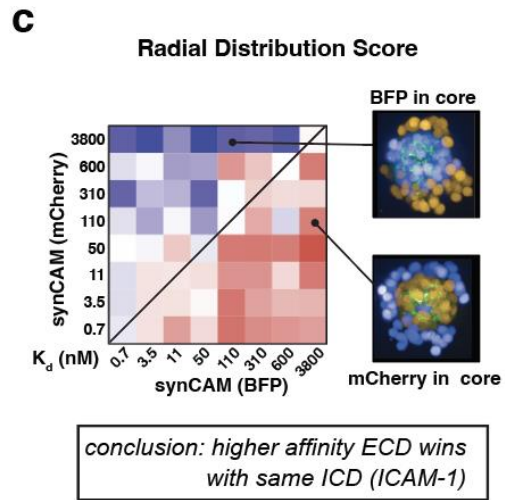
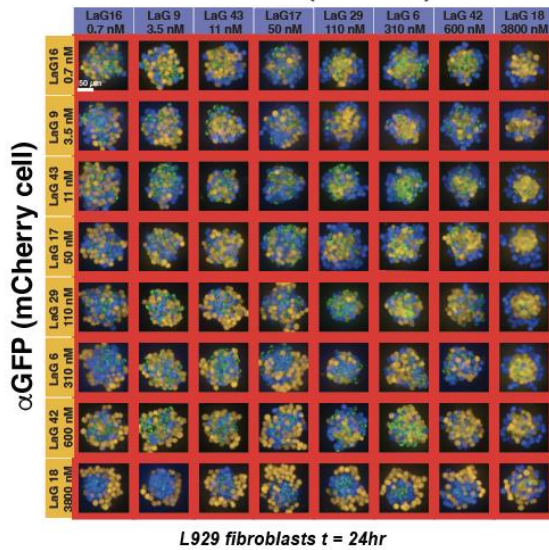
**(a)** FACS analysis of GFP synCAM and αGFP synCAM expression in L929 fibroblast cells following cell sorting with an ICAM-1 or Tether ICD. For the GFP constructs, expression is shown both for total GFP signal in the cell (left) and cells stained with an αFlag APC 647 antibody (middle).

**(b)** Maximum projection of 20X confocal microscopy images of pairwise synCAM interfaces ( $t = 3$  hr) of different expression levels from **panel a**: GFP-expressing cell (blue) is bound to an αGFP expressing cell (orange). The CAM TM and ICD domain for each pair is ICAM-1 or Tether.

**(c)** Box and whisker plots of contact angles measured from the interfaces shown in **b** ( $n = 10$  pairs error = 95 % CI).



**b sorting competition assay images**  
Vary ECD affinity (ICAM-1 ICD)  
 $\alpha$ GFP (BFP cell)



**d sorting competition assay tether vs iCAM-1 synCAM**

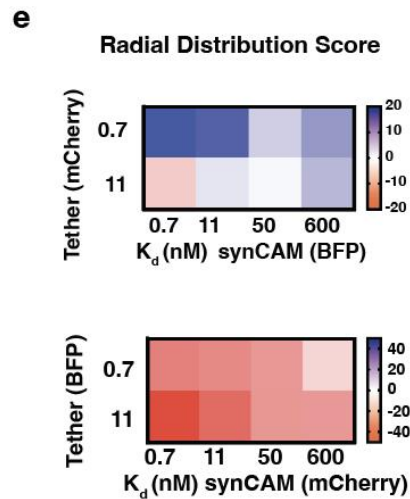
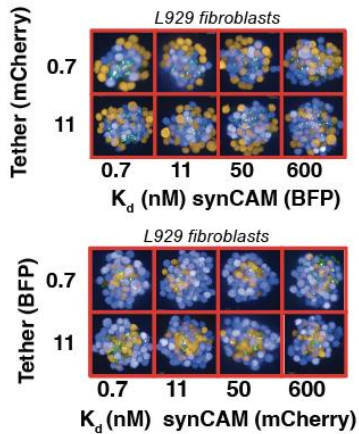


**Figure 2.9. Differential sorting of synCAMs with varying ECD affinity and ICD**  
*(linked to main Fig. 1f)*

**(a)** Cartoon depiction of the differential sorting competition assay (left) and quantification of radial distribution that is represented as a heat map (right). This experiment represents an alternative way to measure adhesion preferences/strength of the diverse synCAM driven cell-cell interactions that differs from the contact angle measurement shown in **Fig. 1f**. Here we mix surface GFP L929 cells (bait cells) with two competing differentially labelled L929 cells, each with a different aGFP synCAM. Stronger adhesion of the synCAM is assessed via the relative degree of co-sorting of the competitor cells to the core in conjunction with the bait cells. We calculate the radial distribution of competing cells (red/blue) from the centroid of the spheroid.

**(b)** Representative maximum projection images of cell sorting competition assay between L929 cells expressing  $\alpha$ GFP-ICAM-1 with the indicated ECD LaG nanobody (mCherry or BFP) mixed with L929 cells expressing GFP-ICAM-1 (t = 24 hr).

**(c)** Quantification of the cell sorting competition assay from **b**.

**(d)** Representative maximum projection images of cell sorting competition assay between L929 cells expressing  $\alpha$ GFP-ICAM-1 and cytosolic and L929 cells expressing  $\alpha$ GFP-Tether mixed with L929 cells expressing GFP-ICAM-1 (t = 24 hr).

**(e)** Quantification of the cell sorting competition assay from **d**.



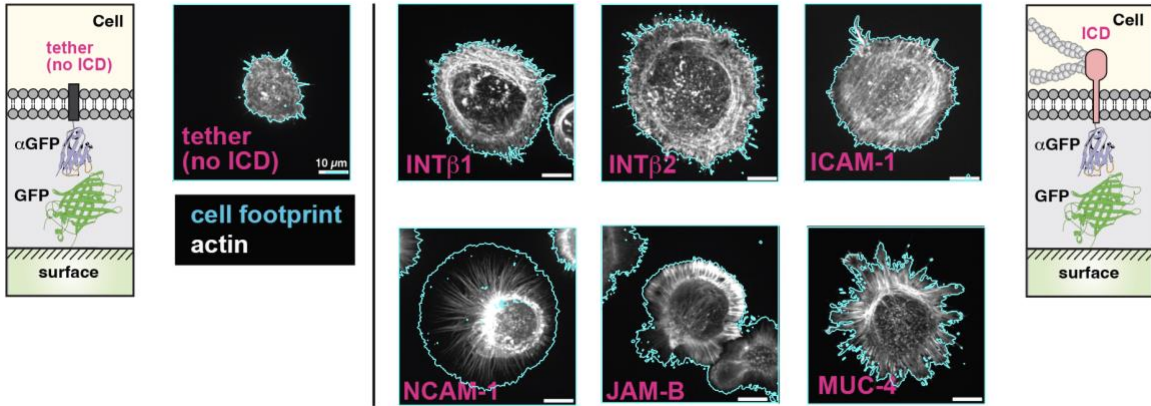


**Figure 2.10. Cell spreading with alternative synCAMs (linked to main Fig. 2)**  
 Example microscopy images of cell spreading assays from Fig. 2, showing phenotypes for all synCAM species. Label indicates ICD used in each synCAM. SynCAMs are expressed in L929 fibroblasts and plated on a GFP coated glass surface. Cell footprint detected by membrane dye is indicated in blue outline; actin as stained by phalloidin and shown in white.

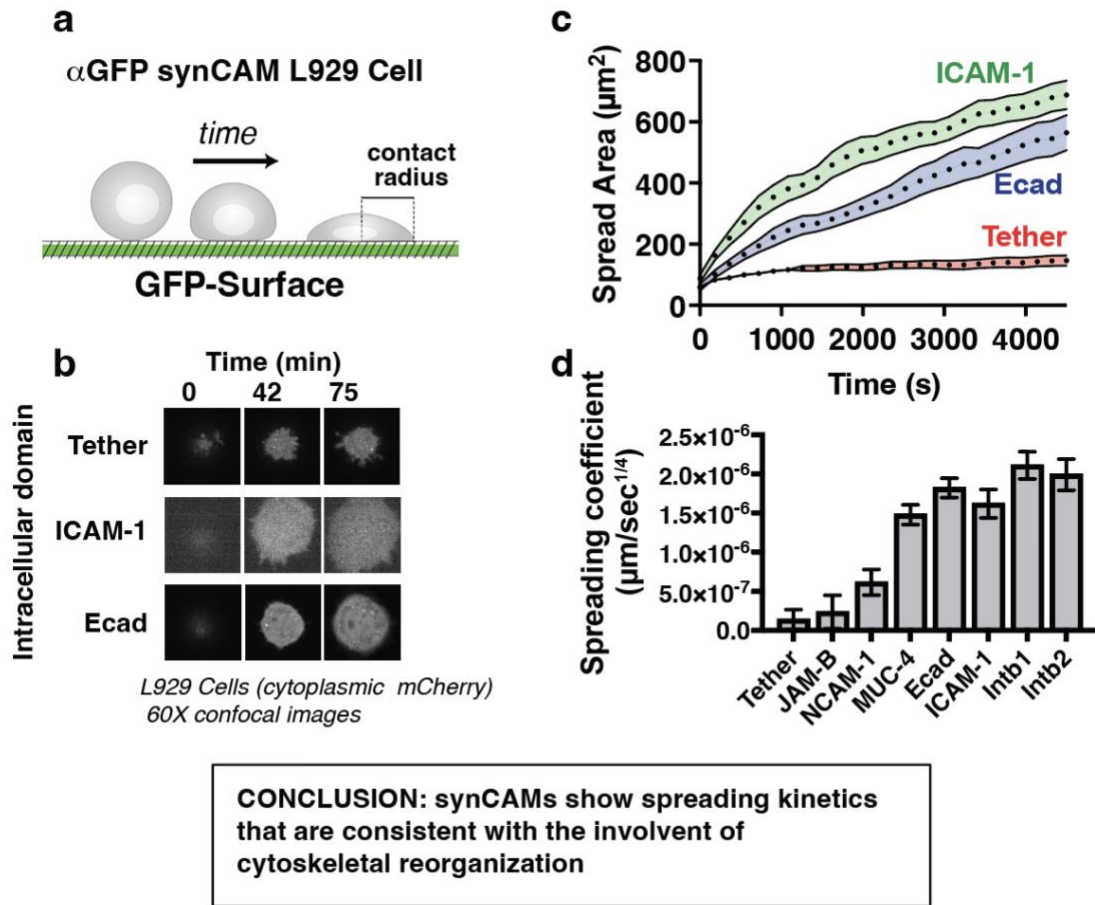


**Figure 2.11. Quantification of synCAM cell spreading kinetics**

**(a)** Cartoon depicting the cell-spreading assay. L929 cells expressing an  $\alpha$ GFP synCAM are plated on a GFP-coated surface and monitored over time.

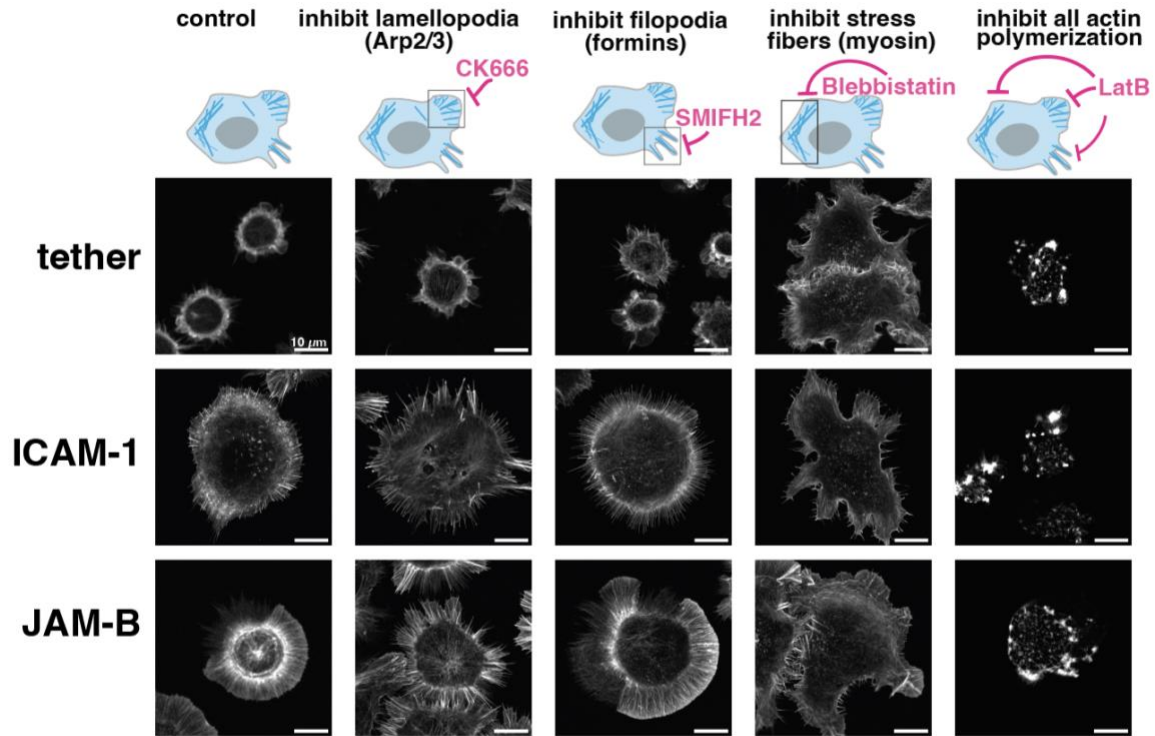
**(b)** Represented images from cell spreading assay of L929 cells expressing the indicated synCAMs. Individual slices from confocal images are shown.

**(c)** Representative cell spreading contact area progress curves of L929 cells expressing the indicated synCAMs. Error = SEM.

**(d)** Calculated spreading constants for L929 cells expressing the indicated synCAMs (n= 12-24 Error = SEM).

These results show that the slow phase of synCAM mediated spreading occurs on the 30-50 minute timescale, consistent with a requirement for major cytoskeletal rearrangements.





**CONCLUSION:** Lamellopodial morphology of JAM-B synCAM appears to be dependent on Arp2/3 mediated actin polymerization pathways

**Figure 2.12. Perturbation of synCAM morphology by small molecule inhibitors of specific actin regulators.** Example microscopy images of L929 fibroblasts expressing  $\alpha$ GFP JAM-B, ICAM-1, or Tether spreading on a GFP coated surface and stained with phalloidin. Spreading is shown in the presence of the indicated inhibitor of actin regulation.



**Figure 2.13. Loss of function mutations in synCAM ICDs**

**(a)** Maximum projection confocal images, and calculated contact angles of synCAM interfaces containing the ICAM-1 ICD with mutations in the ERM binding domains (BD) (n = 20 pairs).

**(b)** Maximum projection confocal images, and calculated contact angles of synCAM interfaces containing the Intb1 ICD with mutations in the two “NPxY” talin binding domain motifs (n = 20 pairs).

**(c)** Maximum projection confocal images, and calculated contact angles of synCAM interfaces containing the Intb2 ICD with mutations in the two “NPxF” talin binding domain motifs (n = 20 pairs).

**(d)** Maximum projection confocal images, and calculated contact angles of synCAM interfaces containing the Ecad ICD with mutations in the b -catenin binding domain (n = 20 pairs).

**(e)** Maximum projection confocal images, and calculated contact angles and GFP enrichment of synCAM interfaces containing the MUC-4 ICD with mutations in Ser and Tyr phosphorylation sites (n = 20 pairs).

**(f)** Maximum projection confocal images, and calculated contact angles and GFP enrichment of synCAM interfaces containing the JAM ICD with mutations in the PDZ binding domain (n = 20 pairs).

**(g)** Maximum projection confocal images, and calculated contact angles and GFP enrichment of synCAM interfaces containing the NCAM-1 ICD with mutations in the Cys palmitoylation site (n = 20 pairs).

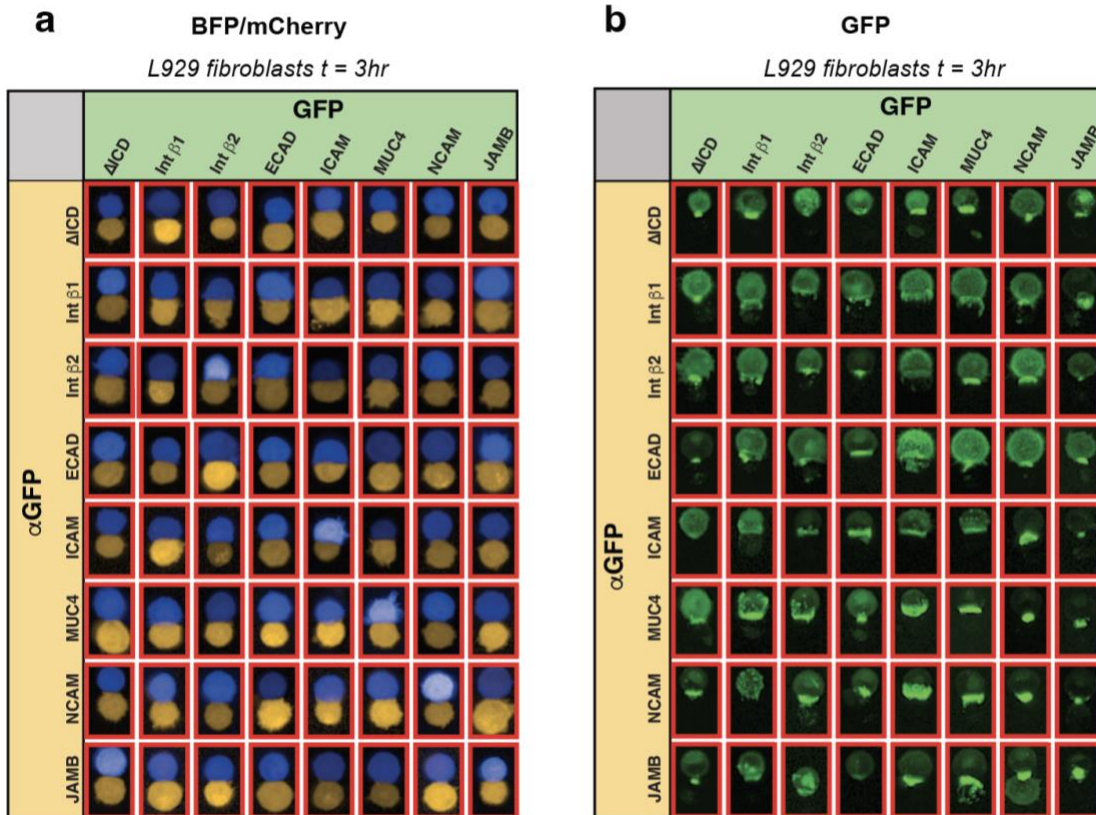
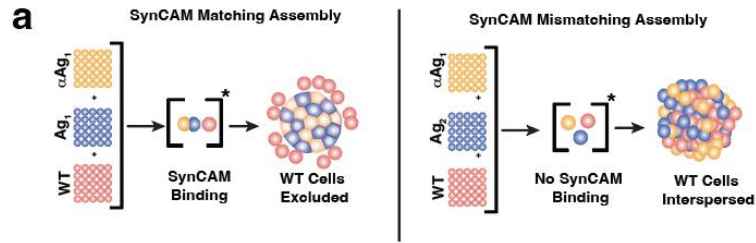


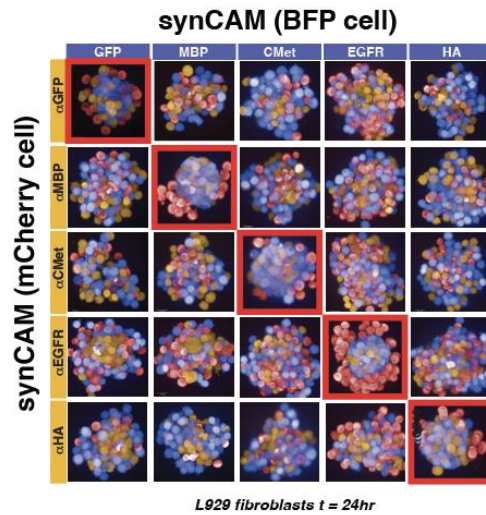
**Figure 2.14. Asymmetric cell-cell interfaces: mismatched ICs**

**(a)** Maximum projection of 20x confocal microscopy images of pairwise synCAM interfaces ( $t = 3\text{ hr}$ ): GFP-expressing cell (blue) is bound to an  $\alpha$ GFP expressing cell (orange) containing the indicated CAM ICD.

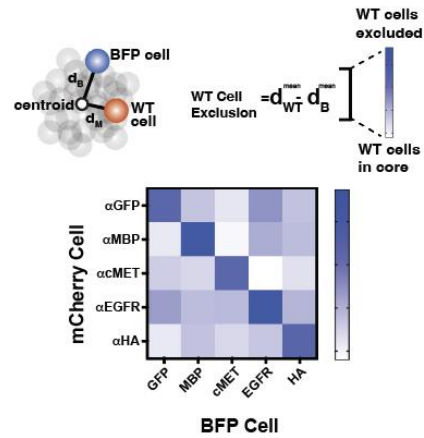
**(b)** GFP channel of cell pairs shown in **a**.



**b** extracellular interaction: variable  
constant intracellular domain: ICAM-1



**c** radial distribution scores



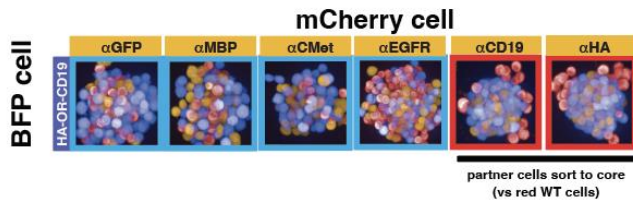
**CONCLUSION: Orthogonal ICAMs are specific for correct partner ICAM**

**d** Bivalent OR-gate synCAM

Epitope 1 Epitope 2 TM/ICD

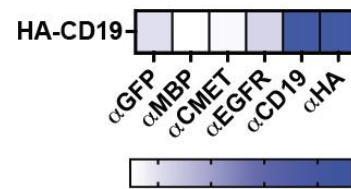
HA CD19 ICAM-1

synCAM Identity in each cell type (BFP vs mCherry) is indicated by labels



**e**

radial distribution scores



**CONCLUSION: OR-gate synCAM assembles preferentially with either αCD19 or αHA partner synCAM**

## Figure 2.15. Testing orthogonality of synCAM ECD pairs by sorting assays

**(a)** Cartoon depicting differential sorting assay used to determine orthogonality of synCAM ECD pairs. SynCAM pairs are mixed with parental L929 cells and imaged after 24 hours. Sorting of parental cells should only occur if the cognate synCAM ECDs are correctly matched and able to bind.

**(b)** Representative maximum projection images of differential sorting assay for a subset of the synCAMs with orthogonal ECDs. Parental L929 cell sorting was only observed in the case of matching ECDs.

**(c)** Quantification of sorting from **b**. The difference of average distance from the center of the sphere between parental L929 cells and BFP+ cells were calculated and are represented as a heat map. Exclusion of parental cells is observed in the case of matching synCAM pairs.

**(d)** Representative maximum projection images synCAM design containing multiple epitopes within a single ECD. The HA-CD19 ECD exhibits differential sorting for either  $\alpha$ CD19 or  $\alpha$ HA synCAMs only. Thus, we can generate OR-gate synCAMs capable of pairing with multiple adhesion partners.

**(e)** Quantification of sorting from **d**. The difference of average distance from the center of the sphere between parental L929 cells and BFP+ cells were calculated and are represented as a heat map. Exclusion of parental cells is observed in the case of matching synCAM pairs.



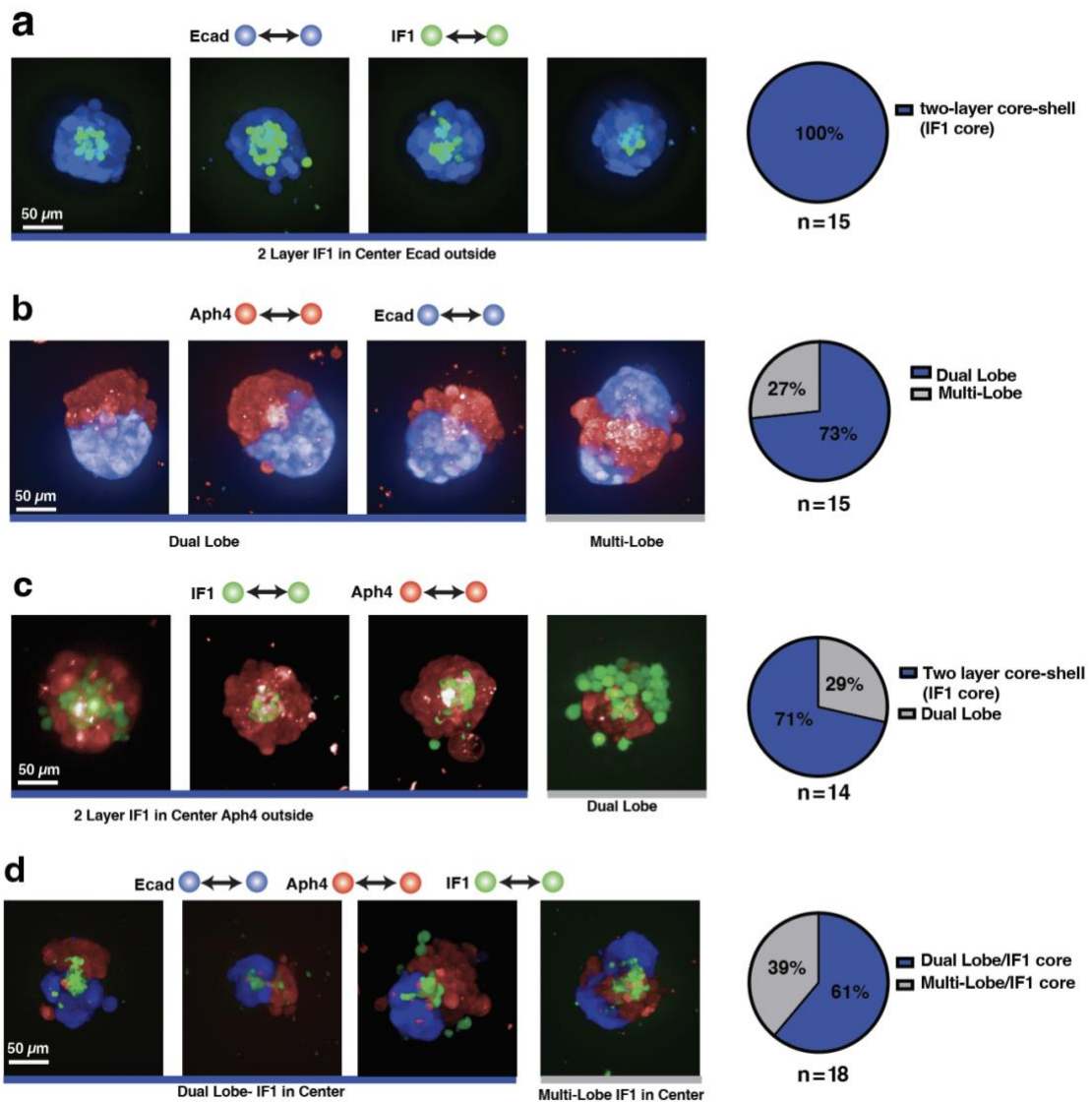


**Figure 2.16 Differential sorting of L929s with homophilic-binding synCAMs**  
 Maximum projection of 20X confocal microscopy images of differential sorting between L929 cells expressing WT Ecad or the indicated homophilic-binding synCAMs ( $t = 48$  hr). Representative images, assembly classifications and distributions are shown for Ecad-IF1 (**a**), Ecad-Aph4 (**b**), IF1-Aph4 (**c**) and Ecad-IF1-Aph4 (**d**).

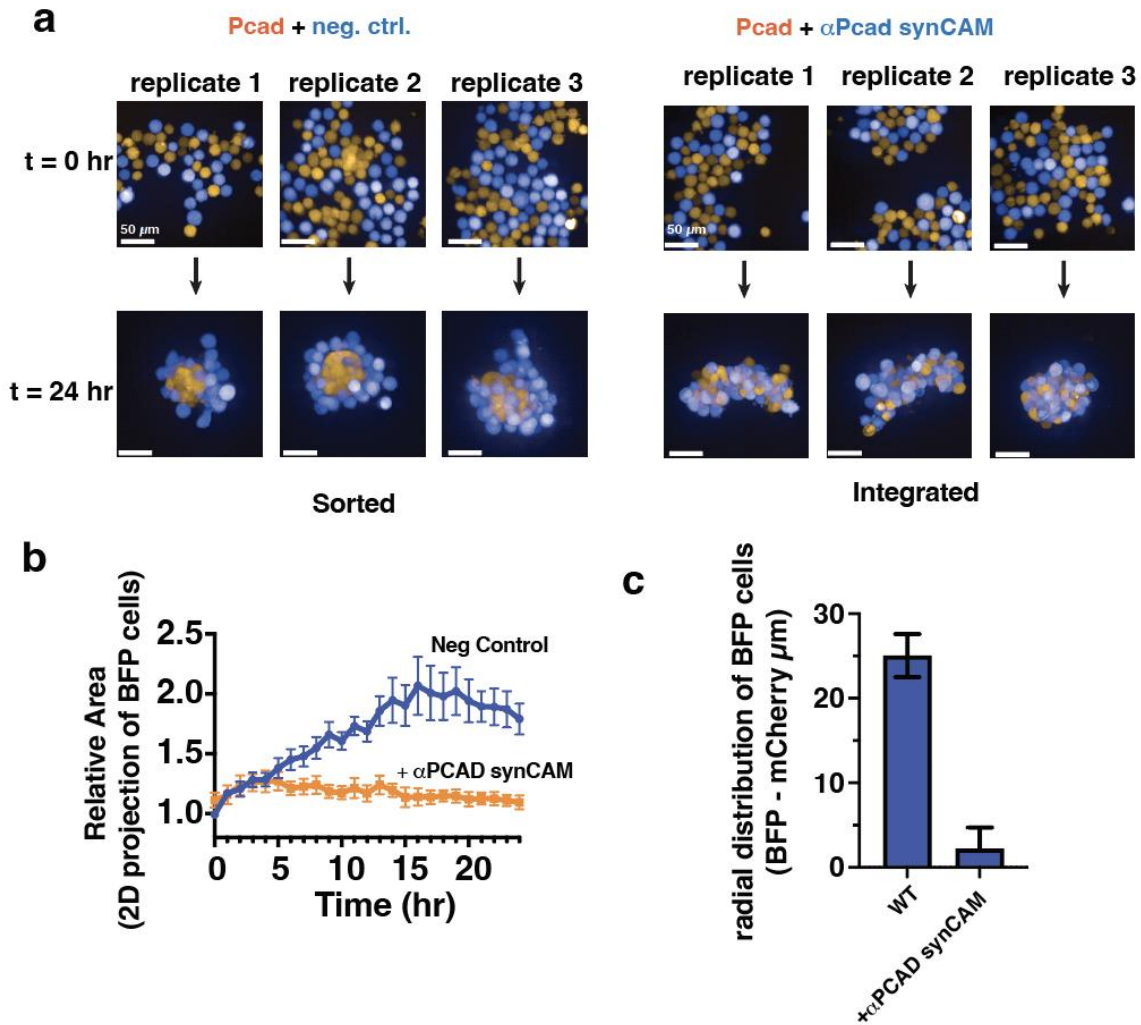


**Figure 2.17. Targeting WT Pcad with synCAM (linked to main Fig. 4e)**

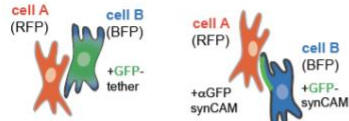
**(a)** Maximum projection images of the sorting assay in which L929 cells expressing WT Pcad (orange) are mixed with parental (left) or synCAM (right) I929 cells (blue, t=0, 24 hr).

**(b)** Quantification of the relative area between the BFP negative control or  $\alpha$ Pcad synCAM and mCherry (Pcad) L929 cells over the course of the 24-hour assembly (n = 4, error = SEM). A greater difference in area is consistent with a more compact Pcad sphere and exclusion of BFP+ cells.

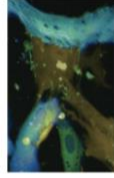
**(c)** Quantification of relative distance per cell (BFP-mCherry) from the center of the sphere following assembly (t = 24 hr, n = 4, error = SEM). WT BFP cells exhibit a greater difference in distance, which is consistent with their exclusion from the Pcad sphere, while  $\alpha$ PCAD synCAMs intercalate.



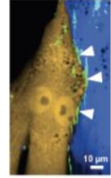
**a** primary mesenchymal stem cells



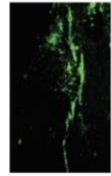
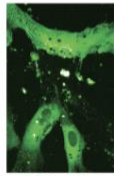
+ tether      + synCAM (ICAM ICD)



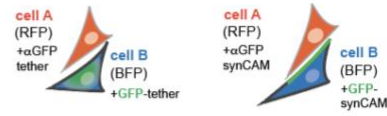
GFP distributed throughout cell B



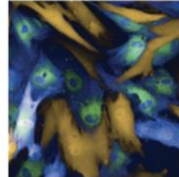
GFP localizes to cell A/B interface (white arrows)



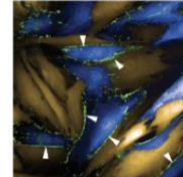
**b** primary dermal fibroblasts



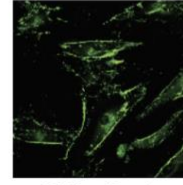
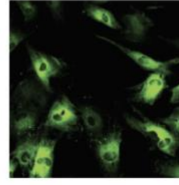
+ tether      + synCAM (ICAM ICD)



GFP distributed throughout cell B

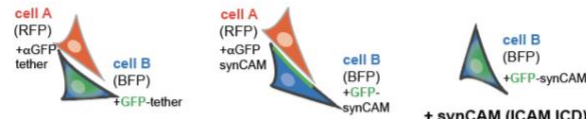


GFP localizes to cell A/B interface (white arrows)

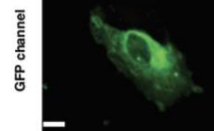
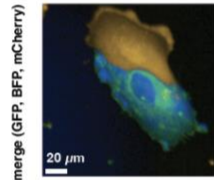


**c**

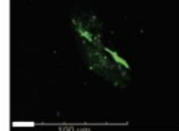
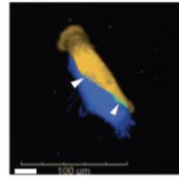
iPSC derived smooth muscle cells



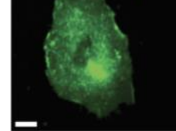
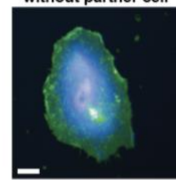
+ tether      + synCAM (ICAM ICD)      + synCAM (ICAM ICD) without partner cell



GFP distributed throughout cell B



GFP localizes to cell A/B interface (white arrows)



GFP distributed throughout cell B

**Figure 2.18. SynCAMs function in primary cells: mesenchymal stem cells (MSCs), dermal fibroblasts, and iPSC derived smooth muscle cells (*linked to main Fig. 4*)**

Maximum projection of 20x confocal microscopy images of  $\alpha$ GFP and GFP synCAMs (with ICAM-1 ICD) or corresponding tether (no ICD) expressed in MSCs (a) primary dermal fibroblasts (b) or iPSC derived SMCs (c).  $\alpha$ GFP cells were also labelled with mCherry; GFP cells were also labelled with BFP. In both cell types, the GFP-tether is diffusely spread throughout the cell. In contrast, the GFP-synCAM is strongly enriched at heterotypic cell-cell interfaces (white arrows). When cells expressing GFP-synCAMs are plated without their partner cells, the GFP is diffusely distributed throughout the cell.

## **Chapter 3- Using synthetic adhesion molecules to enhance cellular CAR-T therapy**

### **Abstract**

Cell adhesion between T cells and their targets plays an essential role in cell killing. Recent studies suggest CAR-T cells are inefficient in exploiting adhesion interaction in inducing T cell activation, which results in low antigen sensitivity (Burton et al., 2023). Furthermore, downregulation of adhesion is a common mechanism by which tumor cells escape killing by both endogenous T cells and therapeutic CAR (chimeric antigen receptor) T cells (Frangieh et al., 2021; Larson et al., 2022; Majzner, Frank, et al., 2020). Theoretically, it may be possible to prevent this adhesion-mediated immune evasion by engineering replacement synthetic adhesion interactions into CAR T cells. We have recently developed a platform of synthetic cell adhesion molecules (synCAM) that can be used to program the attachment of arbitrary cells together with tunable adhesion strength and geometry (Stevens et al., 2023). Here we demonstrate improvement in CAR-mediated killing against tumors with either low CAR antigen density or loss of adhesion molecules using synCAM to induce T cell-tumor interactions.

## Introduction

Adhesion molecules play critical roles in mediating T-cell activities such as trafficking, crawling, and activation (Espie & Donnadieu, 2022; Semmrich et al., 2005; Walling & Kim, 2018). The importance of adhesion interaction in T cell activation has recently garnered attention in the CAR-T field as several studies suggest how tumors can evade CAR-T mediated cytotoxicity by downregulating adhesion molecules T cells normally use to attach and form immunological synapse(Dustin, 2007; Espie & Donnadieu, 2022; Larson et al., 2022).

Furthermore, other studies have shown how inefficient exploitation of adhesion molecules in CAR-T cells may be linked to low antigen sensitivity of CAR-T cells (Burton et al., 2023; Katsarou et al., 2021). While CARs are effective in killing tumors with high levels of CAR antigen, low antigen-expressing tumor cells can escape the CAR-mediated killing. Even the most well-studied aCD19 CARs have been reported to have decreased cytotoxicity against B cells with low CD19 expression(Majzner, Rietberg, et al., 2020).

This problem of suboptimal antigen sensitivity will likely be more prominent as more CAR-T trials will be conducted against solid tumors with immunosuppressive microenvironments which could further dampen the CAR-T mediated cytotoxicity(Heitzeneder et al., 2022; Shiao et al., 2011) With a surplus of data pointing to the importance of adhesion interaction in CAR-mediated killing, we devised a novel strategy to induce synthetic adhesion between T cells and tumor cells using a recently developed synthetic cell adhesion molecules (synCAMs)(Stevens et al., 2023).

## RESULTS

### *Using cell synthetic adhesion molecules (synCAMs) to enhance CAR-T mediated cytotoxicity*

We first generated an array of synthetic adhesion molecules (synCAMs) by fusing aGFP-nanobody(Lag16) to transmembrane and intracellular domains of diverse adhesion molecules including ICAM, NCAM, LFA1, VLA4 as well as the tether control without any intracellular domain. These constructs were then co-transduced with Cetuximab-based aEGFR CAR in human primary CD8+ T cells. Sorted T cells were co-cultured with the MCF7 breast cancer cell line which was engineered to express GFP on the surface as the model antigen for synthetic cell adhesion molecules (**Fig. 3.1a**).

MCF7 cells express surface EGFR at a low level that is below the threshold at which aEGFR-CAR is able to recognize and effectively kill the MCF7 cell line. However, T cells expressing synthetic adhesion molecule with NCAM transmembrane and intracellular domains (synNCAM) and aEGFR CAR, were able to kill the MCF7 cells much more efficiently. While other synthetic adhesion molecules made with ICAM, LFA1, VLA4 had varying levels of improvement, synNCAM consistently had the most significant enhancement in the CAR-mediated killing of MCF7. To account for the interaction between the anti-GFP binder(lag16) and GFP, tether control with no ICD was also transduced with aEGFR-CAR, and demonstrated to have no enhancement in CAR-mediated killing (**Fig 3.1b**).

T cells used in the killing assay were then stained for both early T cell activation marker CD69 and late T cell activation marker CD25. At 2 days after co-culture, T cells expressing both synCAM and aEGFR showed elevated expression of both CD69 and

CD25 compared to the T cells only expressing aEGFR CAR or T cells expressing aEGFR CAR and other synCAMs (**Fig 3.1c**). Additionally, T cells expressing only synNCAMs had similar activation levels as untransduced T cells (data not shown), suggesting interactions of both aEGFR CAR and synNCAM are required to induce T cell activation.

### ***Using synthetic adhesion molecules to exclude CD45 from T cell immunological synapse***

The mechanism behind synthetic NCAM specific enhancement in CAR-mediated killing was not clear because synthetic NCAM was reported to induce high polarization instead of inducing tight adhesion when expressed in L929 fibroblast cells(Stevens et al., 2023). NCAM is normally expressed on the surface of neuronal cells and natural killer cells (Stocum, 2012). Also known is the role of NCAM in cell polarization of NK cells during granule externalization(Viswanath et al., 2017).

The reported importance of NCAM in cell polarization led us to investigate the effect synNCAM has on the immunological synapse. While there are a handful of surface molecules found at the T cell immunological synapse, we decided to investigate the effects synNCAM has on the CD45, for exclusion of CD45 from the center of immunological synapse has been linked to efficient TCR signaling, and TCRs are reported to be superior in targeting tumors with low target antigen density(Burton et al., 2023; Jung et al., 2021).

To visualize the localization of CD45 in respect to immunological synapse, T cells expressing synNCAM, synICAM and tether against GFP were stained with aCD45

antibody with a conjugated fluorophore and then co-cultured with MCF7 cells expressing GFP-ICAM. After 3 hours of co-culture, T cells were imaged for CD45 using a confocal microscope. As a result, T cells expressing synNCAM were shown to exclude CD45 from the interface between T cell and the target MCF7 cells. In contrast, T cells expressing either synICAM or tether controls did not show any exclusion of CD45 from the immunological synapse (**Fig. 3.2a,b**).

This finding inspired us to investigate the effect of varying extracellular lengths of synCAMs on the CD45 exclusion, for lengths of extracellular domain of CARs have been previously reported to play an important role in excluding CD45 from the immunological synapse (Xiao et al., 2022). In imaging CD45 exclusion, synNCAM with a longer extracellular domain (5 Ig repeats of ICAM) was not able to exclude CD45 from the immunological synapse (**Fig. 2a,b**), suggesting that longer receptor makes kinetics of excluding CD45 less favorable (**Fig 3.2c**).

To study whether loss of function in excluding CD45 will translate to loss of enhancement in CAR-mediated killing, synNCAMs with various extracellular lengths (Ig1-Ig5) were co-transduced with aEGFR CAR in T cells and co-cultured with MCF7 expressing GFP-ICAM. With increasing lengths of the extracellular domain, there was decrease in enhancement in CAR-mediated killing (**Fig 3.2d**).

### ***Targeted tumor eradication in mouse model using synthetic cell adhesion molecules***

To determine the feasibility of using synthetic adhesion molecules for improved CAR-mediated killing, we designed a mouse experiment using the MCF7 cells. NSG

mice were subcutaneously implanted with WT MCF7 cells in the left flank and GFP-ICAM+ MCF7 cells in the right flank. These mice were then treated with T cells expressing aEGFR CAR with and without synNCAM and tether control against GFP (**Fig 3.3a**). Then tumor size of both flanks was measured using a caliper twice a week. After 7 days post-T cell injections, group that was treated with T cells expressing aEGFR CAR and aGFP-synNCAM started to selectively kill the GFP-ICAM+ flank tumor, and controlled the tumor growth until the termination of the in-vivo experiment. In contrast, all other groups showed no control of tumor in either of the flanks (**Fig. 3.3b**). With viable proof of principle in both in-vitro and -vivo, we decided to explore endogenous molecules on MCF7 cells that we can use as a target antigen for synNCAM. In screening for candidates for endogenous target molecules, high expression levels were prioritized. NCAM against L1CAM was generated and transduced in T cells along with aEGFR CAR (**Fig 3.3c**). While T cells expressing synNCAM against L1CAM increased the CAR-mediated killing of MCF7, the extent of enhancement in killing was dampened compared to targeting GFP-ICAM with synNCAM (**Fig 3.3d**).

### ***Using synthetic cell adhesion molecules to restore adhesion interaction between T cells and tumor cells with defective adhesion***

A recent study by Larson et al. demonstrates the importance of having adhesion molecules being expressed on solid tumors for efficient CAR-T-mediated killing (Larson et al., 2022) In the study, IFN $\gamma$ R gene was knocked out from various solid tumors, resulting in loss of ICAM-1 upregulation in the presence of soluble IFN $\gamma$ . We were



curious to test whether synNCAM could restore the CAR-mediated killing in the solid tumor cells with IFNgR knockout. To test this idea, we generated IFNgR KO cell lines for MCF7 breast cancer cells and U87 breast cancer cells (**Fig 3.4a**). Then these IFNgR cell lines were co-cultured with T cells expressing aEGFR in the presence and absence of synNCAM. We were able to confirm the knocking out of IFNgR in solid tumor cells resulting in diminished CAR-mediated killing of the tumor cells (**Fig 3.4b,c**).

Furthermore, we demonstrated that T cells expressing both CAR and synCAMs were not only able to restore the killing to the level of targeting WT MCF7 and WT U87 cell lines but also enhance the killing beyond the level of targeting WT cancer cell lines (**Fig 3.3b,c**).

## **Discussion**

### **Developing CAR-T therapies with increased antigen-sensitivity**

While CAR-T field has seen tremendous success in treating CD19-high B cell lymphoma, there remains the challenge of targeting CD19-low B cell lymphoma, which could lead to antigen escape (Majzner & Mackall, 2018). With a vast number of different solid tumor types that have not been successfully treated with CAR-T therapy, increasing the antigen sensitivity of CAR-T therapy will be beneficial for the field. In this dissertation, we discussed a new synthetic cell adhesion molecule and its application in primary T cells to enhance the antigen sensitivity of CARs. Because of the heterogeneity found in different tumors, implementing this strategy to improve the antigen sensitivity of CAR-T therapy in the clinical setting will require careful analysis of

tumor biopsy profiles. Although not discussed in this dissertation, using synCAMs to induce tissue residency of the engineered T cells is another area of research that could benefit the field. Because T cells use an intricate cascade of inside-out signaling utilizing adhesion molecules, careful engineering, and application of synCAMs could also be used to direct the trafficking of the engineered T cells to specific sites in the body (Slaney et al., 2014; Walling & Kim, 2018).

As we continue engineering different synthetic receptors, we hope to develop novel strategies that can improve not only the CAR-T field but also different areas of research that require creative engineering. In future studies, we hope to further engineer and optimize the synthetic cell adhesion and also other synthetic receptors to improve the dynamic range of the system while maximizing specificity. Synthetic biology offers distinct possibilities to address the challenges faced by the initial generation of T cell therapies. We believe leveraging synthetic biology principles and technology platforms will empower the broader scientific community to develop enhanced and pioneering T cell therapies.

## References

- Burton, J. et al. Inefficient exploitation of accessory receptors reduces the sensitivity of chimeric antigen receptors. *Proceedings of the National Academy of Sciences*, 120(2), (2023).
- Dustin, M. L. Cell adhesion molecules and actin cytoskeleton at immune synapses and kinapses. *Current Opinion in Cell Biology*, 19(5), 529–533. (2007).
- Espie, D. & Donnadieu, E. New insights into CAR T cell-mediated killing of tumor cells. *Frontiers in Immunology*, 13, 1016208 (2022).
- Frangieh, C. et al. Multimodal pooled Perturb-CITE-seq screens in patient models define mechanisms of cancer immune evasion. *Nature Genetics*, 53(3), 332–341(2021).
- Heitzeneder, S. et al. GPC2-CAR T cells tuned for low antigen density mediate potent activity against neuroblastoma without toxicity. *Cancer Cell*, 40(1) (2022).
- Jung, Y., Wen, L., Altman, A. & Ley, K. CD45 pre-exclusion from the tips of T cell microvilli prior to antigen recognition. *Nature Communications*, 12 (2021).

Katsarou, A et al. Combining a CAR and a chimeric costimulatory receptor enhances T cell sensitivity to low antigen density and promotes persistence. *Science Translational Medicine*, 13(623), (2021).

Larson, R. et al. CAR T cell killing requires the IFN $\gamma$ R pathway in solid but not liquid tumours. *Nature*, 604(7906), 563–570 (2022).

Majzner, R. et al. CD58 Aberrations Limit Durable Responses to CD19 CAR in Large B Cell Lymphoma Patients Treated with Axicabtagene Ciloleucel but Can be Overcome through Novel CAR Engineering. *Blood*, 136(Supplement 1), 53–54(2020).

Majzner, R. G. & Mackall, C. L. (2018). Tumor Antigen Escape from CAR T-cell Therapy. *Cancer Discovery*, 8(10), 1219–1226 (2018).

Majzner, R. Tuning the Antigen Density Requirement for CAR T-cell Activity. *Cancer Discovery*, 10(5), 702–723 (2020).

Semmrich, M et al. Importance of integrin LFA-1 deactivation for the generation of immune responses. *The Journal of Experimental Medicine*, 201(12), (2005).

Shiao, S. et al. Immune microenvironments in solid tumors: new targets for therapy. *Genes & Development*, 25(24), 2559–2572 (2011).

Slaney, C. Y., Kershaw, M. H. & Darcy, P. K. Trafficking of T Cells into Tumors. *Cancer Research*, 74(24), 7168–7174 (2014).

Stevens, A. et al. Programming multicellular assembly with synthetic cell adhesion molecules. *Nature*, 614(7946), 144–152. (2023).

Stocum, D. L. *Regenerative Biology and Medicine (Second Edition)*. Part I: *Regenerative Biology*, *Biochem Biophys Res Comm*2702000, 67–97 (2012).

Viswanath, D. I., Mace, E. M., Hsu, H.-T. & Orange, J. S. Quantification of natural killer cell polarization and visualization of synaptic granule externalization by imaging flow cytometry. *Clinical Immunology*, 177, 70–75 (2017).

Walling, B. L. & Kim, M. LFA-1 in T Cell Migration and Differentiation. *Frontiers in Immunology*, 9, 952 (2018).

Xiao, Q. et al. Size-dependent activation of CAR-T cells. *Science Immunology*, 7(74), eabl3995. (2022).

## **Methods**

### ***Primary Human T Cell Isolation and Culture***

Primary CD4+ and CD8+ T cells were isolated from anonymous donor blood after apheresis by negative selection (STEMCELL Technologies #15062 and #15063). Blood was obtained from Blood Centers of the Pacific, as approved by the University Institutional Review Board. T cells were cryopreserved in RPMI-1640 (UCSF cell culture core) with 20% human AB serum (Valley Biomedical, #HP1022) and 10% DMSO. After thawing, T cells were cultured in human T cell medium consisting of X-VIVO 15 (Lonza #04-418Q), 5% Human AB serum, and 10 mM neutralized N-acetyl L-Cysteine (Sigma-Aldrich #A9165) supplemented with 30 units/mL IL-2 (NCI BRB Preclinical Repository) for all experiments except for the IncuCyte experiments. IncuCyte experiments were cultured in RPMI-1640 (UCSF cell culture core) with 10% human AB serum (Valley Biomedical, #HP1022)

### ***Lentiviral Transduction of Human T Cells***

Pantropic VSV-G pseudotyped lentivirus was produced via transfection of Lenti-X 293T cells (Clontech #11131D) with a pHR'SIN:CSW transgene expression vector and the viral packaging plasmids pCMVdR8.91 and pMD2.G using Fugene HD (Promega #E2312). Primary T cells were thawed the same day and, after 24 hr in culture, were stimulated with Human T-Activator CD3/CD28 Dynabeads (Life Technologies #11131D) at a 1:3 cell:bead ratio. At 48 hr, viral supernatant was harvested and in some assays concentrated using Lenti-X concentrator (Clonetechn #631231). The primary T cells were exposed to the virus for 24 hr. At day 4 after T cell stimulation, the Dynabeads were

removed, and the T cells were expanded until day 9 when they were rested and could be used in assays. T cells were sorted for assays with a Beckton Dickinson (BD) FACs ARIA Fusion. AND-gate T cells exhibiting basal CAR expression were gated out during sorting.

### ***Cancer Cell Lines***

The cancer cell lines used were MCF7 breast cancer cell line (ATCC #HTB-22) and U87MG GBM cells (ATCC #HTB-14). Both MCF7 and U87 cells were lentivirally transduced to stably express either surface GFP (GFP fused to the PSGL transmembrane domain) or surface GFP-ICAM (GFP-fused to the transmembrane and intracellular domain of ICAM). GFP peptide sequences can be found in Morsut et al. (Morsut et al., 2016). Both MCF7 and U87 cell lines were lentivirally transduced to express cytosolic mCherry. All cell lines were sorted for expression of the transgenes.

### ***Cytotoxicity assays***

IncuCyte Live Cell Analysis recorded the total red area for tumor cells as a readout of remaining tumor cells. Adherent tumor cells were plated at low confluency one day prior to T cell addition to allow growth of the tumor lines during the course of the experiment. At the end of the experiment, the total red area of each well at different timepoints was normalized to the total red area of each well at time zero. Then these values were plotted to show the growth of tumor cells over time. CAR T cells were added at either a 1:1 E:T or 1:2 E:T ratio.

### ***Mouse models***

All mouse experiments were conducted according to Institutional Animal Care and Use Committee (IACUC)–approved protocols

The 6-8 week old female NSG mice (Charles river), with 5-7 mice per group. In MCF-7 xenograft model, a slow-release pellet containing 0.36 mg of 17 $\beta$ -estradiol (Innovative Research of America, Sarasota, USA) was subcutaneously implanted into the back of nude mice 1 day prior to the xenograft implantation. For orthotopic xenograft models, the cells suspended in PBS were mixed at 1:1 with Matrigel (Corning, USA). The mixed cells were injected subcutaneously into both flanks. Xenograft growth rates were analyzed by measuring tumor length (L) and width (W), and calculating volume through the use of the formula  $LW^2/2$ . For tail vein injection of T cells, the cells suspended in PBS were injected into the lateral tail vein of mice.

### ***CD45 exclusion measurements***

1e6 T cells were stained in 100ul at 1:50 dilution of Anti-CD45 Mouse Monoclonal Antibody (APC (Allophycocyanin)) [clone: HI30] for 25 min in 4 degrees Celsius. After adding 1ml of DPBS, samples were centrifuged for 4 min at 400 x g then T cells were resuspended at 100,000 cells/ml in cold RPMI+10% FBS. 8,000 MCF7 expressing GFP-ICAM on the surface were seeded on 384 Cellstar® Tissue Culture Plates, Greiner Bio-One 6 hours prior in 40ul DMEM+10% FBS. Then 4,000 T cells stained with aCD45 antibody were added to the wells containing MCF7 cells in 40ul volume. After 3 hours of co-culture, 40ul of the liquid was gently removed from the wells, then 40ul of 8% PFA was added to each well then incubated for 2 hours in the



dark at 4 degrees Celsius. Then PFA was replaced with PBS and the plate was imaged at 63x magnification using fluorescence confocal microscopy (Phenix). Images were then exported as TIFF files and further analyzed in ImageJ for average fluorescence intensity of CD45 signal at the cell-cell interface and across the periphery of the T cell, respectively. Mean fluorescence intensity of CD45 signal at the interface was then divided by the fluorescence intensity of CD45 signal across the periphery of T cells. This value was then plotted to show how much CD45 was excluded at the interface, with lower number indicating more CD45 exclusion.

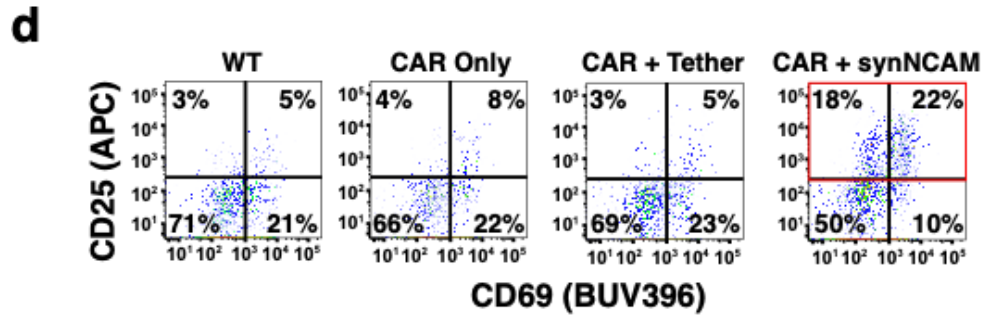
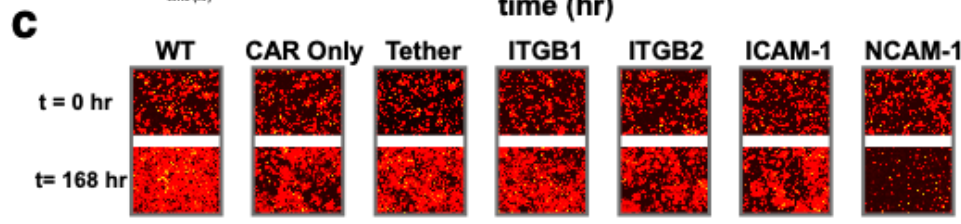
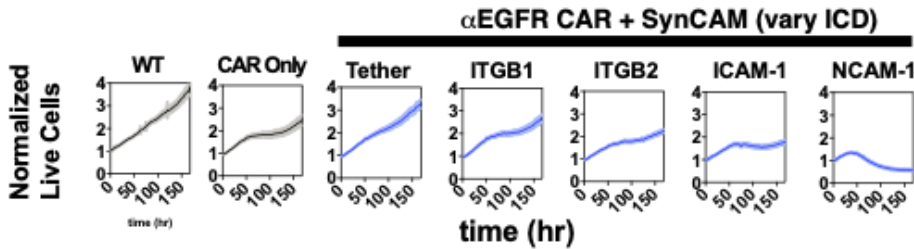
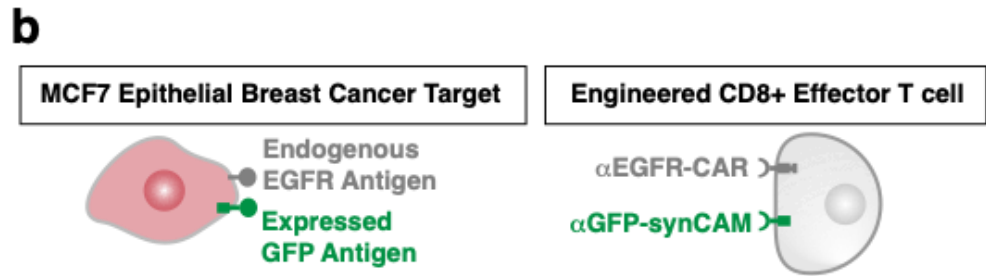
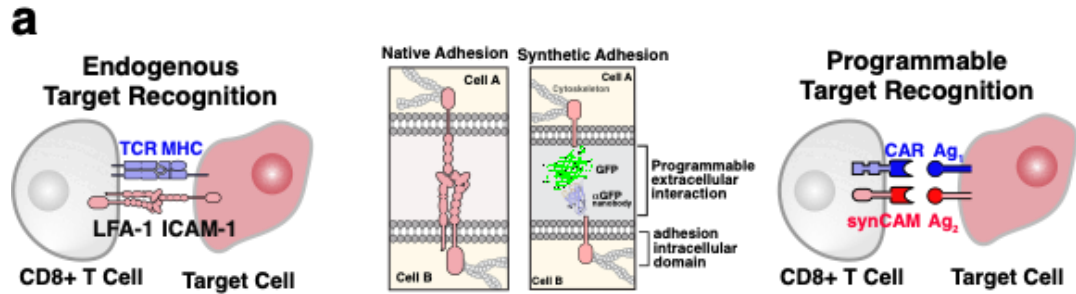


### Figure 3.1. SynCAMs improve CAR T cell killing

**(a)** Conceptual design of synthetic cell adhesion molecule (synCAM) CAR T cells. Left: Depiction of endogenous T cell adhesion mediated by lymphocyte function-associated antigen 1 (LFA-1) binding intercellular adhesion molecules (ICAM-1). Middle: Chimeric design of synCAMs: the extracellular domain of a CAM is replaced by a programmable binding interaction. Right: Dual programming of killing (CAR-Ag1) and adhesion (synCAM-Ag2) in an engineered T cell.

**(b)** SynCAM-assisted CAR T Cell killing of MCF7 Target cells. The purpose of this experiment is to identify the optimal synCAM ICD for enhancing CAR T cell killing (in vitro). In this experiment, GFP is expressed on the surface of MCF7 cells (they endogenously express EGFR) and they are cultured in a 96 well flat bottom plate. They are mixed with CD8+ T cells expressing an aEGFR CAR and a synCAM with the indicated ICD (1:1 ET). Live MCF7 cells are monitored over time by incucyte.

**(c)** Incucyte images at t = 0 and t = 7 days of data from B. MCF7 cells are shown in red.

**(d)** Flow cytometry measurement of CD25 and CD69 expression in CAR T cells for synCAM-aided killing (t = 48 hr). Only synNCAM engagement increases expression of CD25. This activation data is consistent with the killing data in panels b and c. Note on Figure: The GFP-ligand for panels B and C is GFP Tether. These experiments are being carried out again targeting GFP-ICAM to better match the in vivo experiments (see Fig. 3.4)-we expect this will enhance the effect seen for NCAM-enhanced killing.

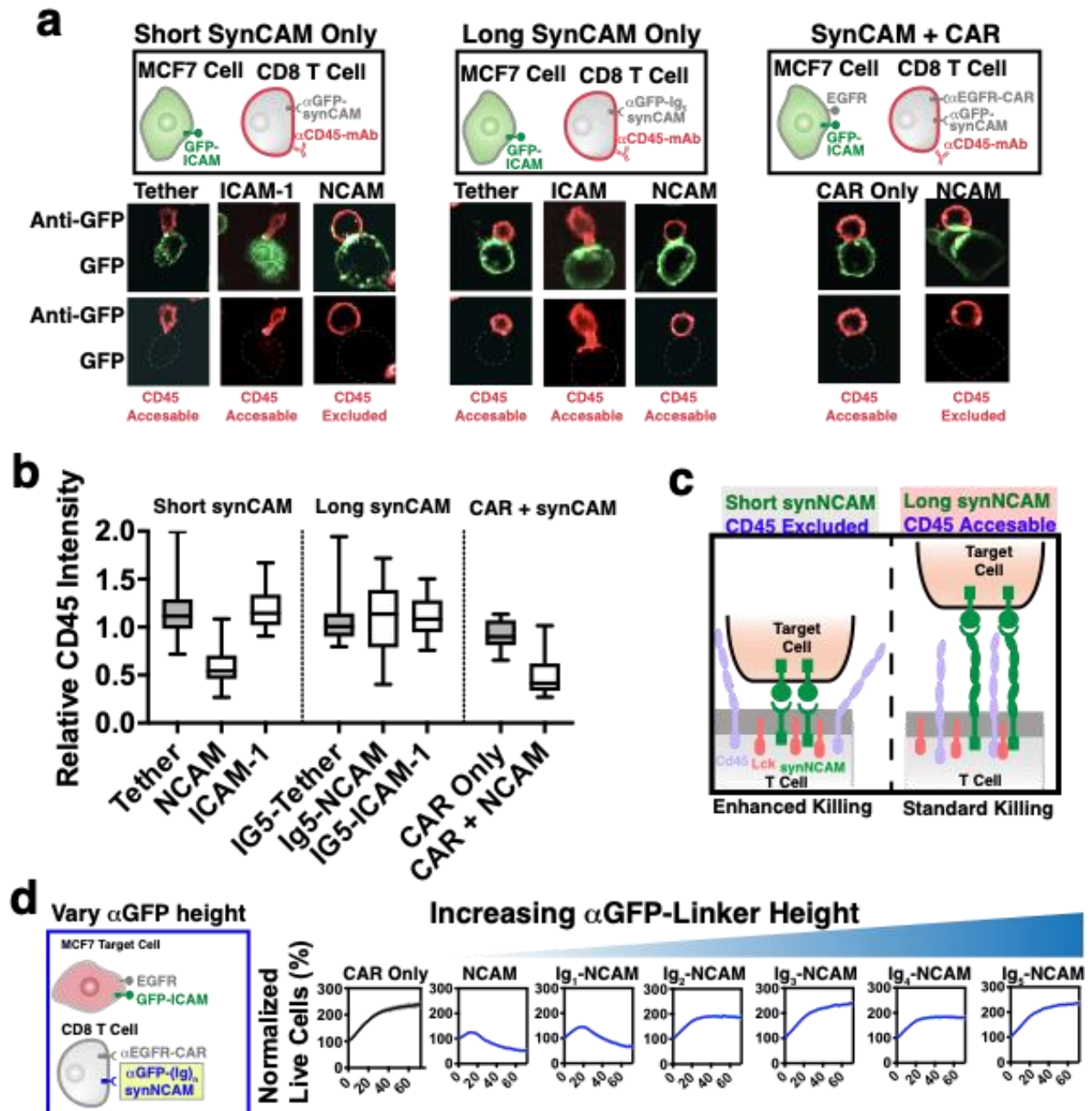


### **Figure 3.2 Short synNCAM facilitates CD45 exclusion**

**(a)** SynNCAM increases CD45 exclusion compared to tether, ICAM, long NCAM. Surface CD45 was stained with a fluorescent-conjugated mAb (red). T cells were mixed with GFP-ICAM+ MCF7 target cells (red or blue). Cells were imaged by confocal microscopy (individual plane shown). CD45 is excluded only on T cells expressing Short synNCAM.

**(b)** Quantification of the images from panel a. Relative CD45 Intensity is the ratio of average CD45 intensity at the cell-cell interface to the average CD45 intensity of the entire cell periphery. Left two images: T cells expressing aEGFR CAR + indicated synCAM. Right three images: T cells expressing indicated synCAM only.

**(c)** Cartoon of synNCAM enabling CD45 exclusion and enhanced killing.

**(d)** Target Killing decreases with increasing synCAM height. Killing of MCF7 cells expressing GFP-ICAM by CAR T cells expressing an aEGFR CAR and synNCAM with an ECD linker domain of varied height (indicated by number of Ig repeats).

**(e)** Target Killing decreases with increasing synCAM Ligand height. Killing of MCF7 cells by CAR T cells expressing an aEGFR CAR and synNCAM. The MCF7 cells are expressing GFP-(Ig)<sub>n</sub>-ICAM, which contain an ECD linker domain of varied height (indicated by number of Ig repeats). Note: This experiment needs to be redone. The poor killing efficiency under all conditions is likely a result of old T cells. Conclusion: synNCAM binding facilitates CD45 exclusion. This effect is height dependant. Note: Additional experiments could be carried out to further support this conclusion.

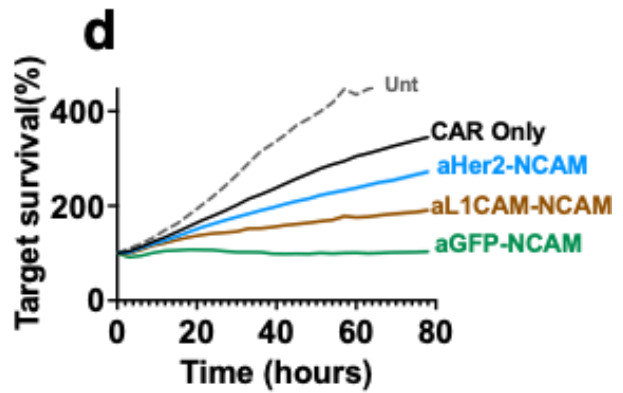
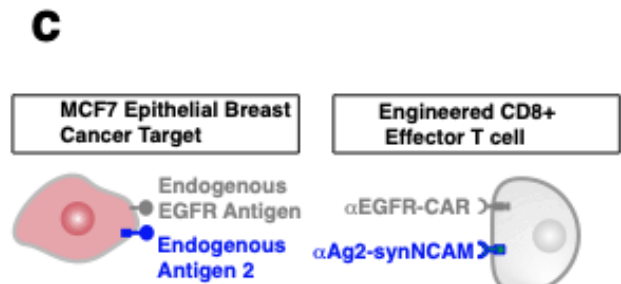
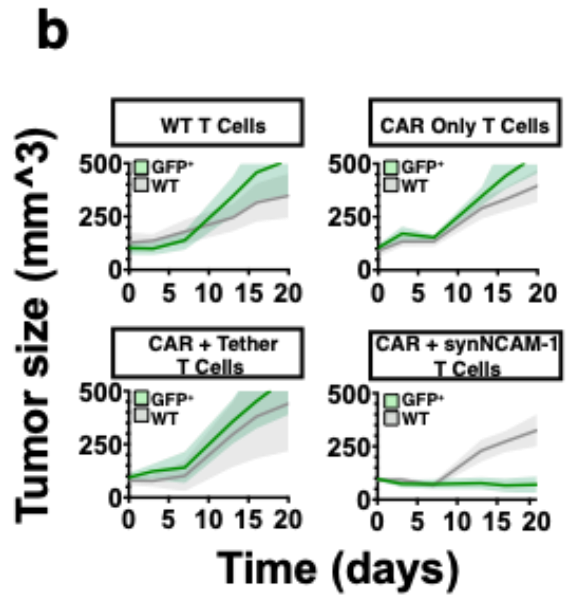
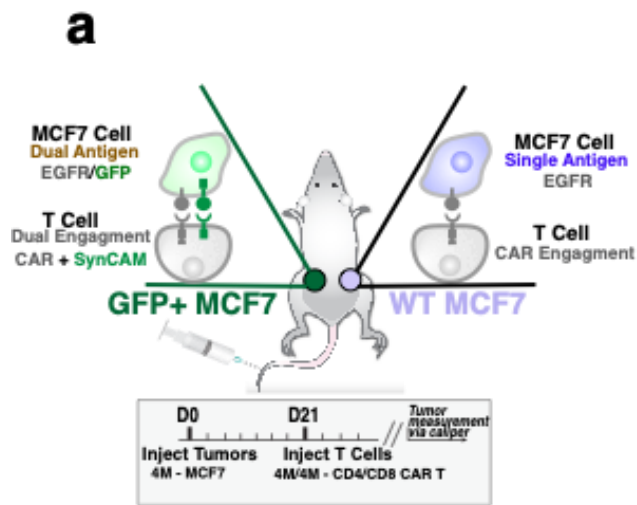


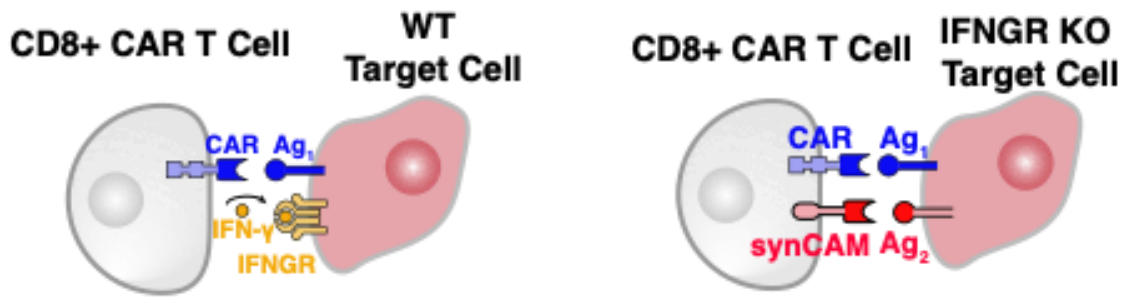
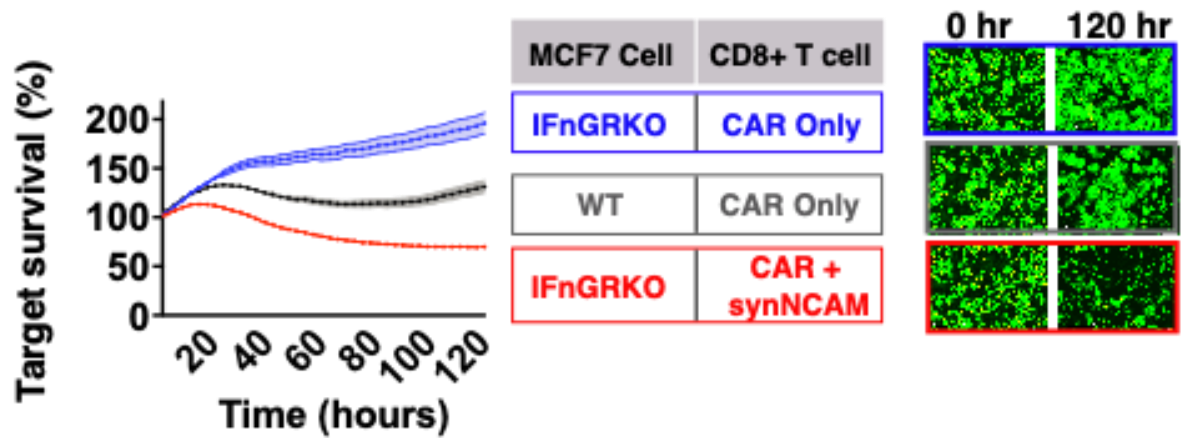
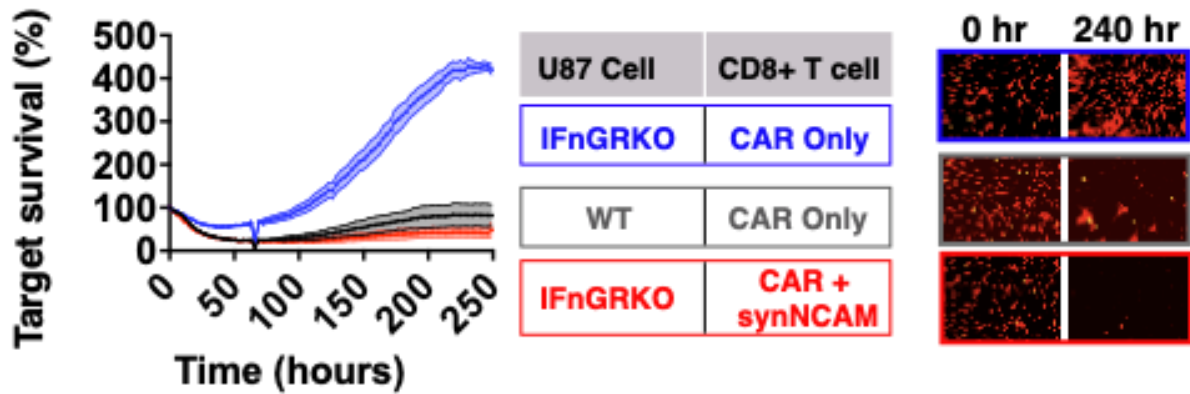
### **Figure 3.3 Enhanced tumor killing in-vivo by synthetic adhesion CAR T cells**

**(a)** Experimental setup of dual flank in vivo tumor model. NSG mice were engrafted with GFP+ (GFP-ICAM, Left Flank) and WT (right flank) MCF7 cells. T cells were injected and tumor size of each flank was quantified via caliper.

**(b)** Tumor killing of GFP+ (Green) and WT (gray) MCF7 flank tumors. Tumor size is shown for mice injected with untransduced (WT), aEGFR CAR Only, CAR + aGFP Tether, and CAR +aGFP-NCAM primary human T cells.

**(c)** Experimental setup of SynCAM Targeting endogenous ligand on MCF7 Cells. WT MCF7 cells are mixed with CD8+ T cells expressing aEGFR CAR and a synNCAM targeting an endogenous ligand.

**(d)** In vitro killing of synCAM CAR T cells targeting endogenous ligand. Survival curves are shown of WT MCF7 cells mixed with aEGFR CAR T cells expressing the indicated synCAM

**a****b****c**



### **Figure 3.4 SynCAM CAR T cells eliminate CAR resistant tumors**

**(a)** Depiction of MCF7 cells with interferon gamma receptor knockout (IFGRKO). These cells exhibit resistance to CAR T cell killing.

**(b)** Survival curve CD8 aEGFR CAR T cells killing IFGRKO MCF7 cells. Loss of interferon gamma receptor increases resistance to CAR T cell killing (blue), which is overcome by introduction of the synNCAM interaction (red ).

**(c)** Survival curve CD8 aEGFR CAR T cells killing IFGRKO U87 cells. Loss of interferon gamma receptor increases resistance to CAR T cell killing (blue), which is overcome by introduction of the synNCAM interaction (red ).

## Chapter 4. Concluding Remarks

In conclusion, this dissertation discusses a novel strategy that can be incorporated to increase the antigen sensitivity of CAR-T therapy. I believe this study will help advance our understanding of how synthetic receptors can revolutionize CAR-T therapy. Throughout this research, we have delved into the intricacies of synthetic biology principles and harnessed the power of different adhesion molecules and distinct phenotypes associated with each adhesion molecule.

By harnessing the power of synthetic receptors, our lab has successfully engineered CAR-T cells with enhanced specificity and precision, enabling them to recognize tumor antigens with greater sensitivity. This breakthrough has the potential to overcome one of the most significant challenges faced by T cell therapies—their limited effectiveness against tumors with low antigen density. The results presented in this dissertation highlight the transformative impact of synthetic biology in the realm of immunotherapy, where the development of improved CAR-T cells offers new hope to patients battling various forms of cancer.

Furthermore, the findings in this dissertation can be used to understand how T cells use different adhesion molecules to form functional immunological synapses. By carefully designing next experiments revolving formation of the functional immunological synapses, I believe we can further optimize CAR-T therapy and make next generation of CAR-T therapy not only more efficacious but also safer. As we continue to optimize and refine these synthetic receptor-based approaches, the broader scientific community will be empowered to engineer innovative T cell therapies tailored to individual patients and their unique cancer profiles. This personalized approach holds the potential to

significantly improve patient outcomes and pave the way toward a more effective and targeted cancer treatment paradigm.

In the broader context of cancer research, I hope the findings presented in this dissertation will contribute to the growing body of knowledge surrounding synthetic biology applications in oncology. As we continue to explore the potential of synthetic receptors and their adaptability, their integration into CAR-T therapy opens the door to a myriad of exciting possibilities for combating not only solid tumors but also hematological malignancies with improved efficacy and reduced side effects.

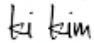
Looking ahead, continued research in the realm of synthetic biology will be crucial to unlocking even greater therapeutic potential. As scientists and clinicians collaborate to further optimize synthetic receptor design and implementation, we can envision a future where CAR-T therapy becomes a mainstream treatment option for cancer patients, delivering personalized, precise, and potent immunotherapeutic interventions.

In conclusion, I hope this dissertation has contributed to paving the way for a brighter future in the fight against cancer. With dedication and innovation, I believe our generation stands poised to transform the landscape of cancer treatment and bring lasting hope to patients and their families worldwide.

## Publishing Agreement

It is the policy of the University to encourage open access and broad distribution of all theses, dissertations, and manuscripts. The Graduate Division will facilitate the distribution of UCSF theses, dissertations, and manuscripts to the UCSF Library for open access and distribution. UCSF will make such theses, dissertations, and manuscripts accessible to the public and will take reasonable steps to preserve these works in perpetuity.

I hereby grant the non-exclusive, perpetual right to The Regents of the University of California to reproduce, publicly display, distribute, preserve, and publish copies of my thesis, dissertation, or manuscript in any form or media, now existing or later derived, including access online for teaching, research, and public service purposes.

DocuSigned by:  
  
B24DDFCB0E064D9... Author Signature

8/14/2023  
Date